Connecting the Deep Earth and the Atmosphere — **Source link** ⤢

Trond H. Torsvik, Trond H. Torsvik, Henrik Svensen, Bernhard Steinberger ...+6 more authors

Institutions: University of Oslo, University of the Witwatersrand, University of Potsdam, Wesleyan University ...+1 more institutions

Related papers:

- Large Igneous Provinces

- Plate tectonics, flood basalts and the evolution of Earth's oceans

- Interplays between magmatism, crustal deformation, surface erosion and long-term climate on the rise and fall of continental arcs

- Invited review Plate tectonics, flood basalts and the evolution of Earth's oceans

- Tectonics: 50 years after the Revolution

Connecting the Deep Earth and the Atmosphere

Trond H. Torsvik[1,2], Henrik H. Svensen[1], Bernhard Steinberger[3,1], Dana L. Royer[4], Dougal A. Jerram[1,5,6], Morgan T. Jones[1] & Mathew Domeier[1]

[1]Centre for Earth Evolution and Dynamics (CEED), University of Oslo, 0315 Oslo, Norway; [2]School of Geosciences, University of Witwatersrand, Johannesburg 2050, South Africa; [3]Helmholtz Centre Potsdam, GFZ, Telegrafenberg, 14473 Potsdam, Germany; [4]Department of Earth and Environmental Sciences, Wesleyan University, Middletown, Connecticut 06459, USA; [5]DougalEARTH Ltd.1, Solihull, UK; [6]Visiting Fellow, Earth, Environmental and Biological Sciences, Queensland University of Technology, Brisbane, Queensland, Australia.

Abstract

Most hotspots, kimberlites, and large igneous provinces (LIPs) are sourced by plumes that rise from the margins of two large low shear-wave velocity provinces in the lowermost mantle. These thermochemical provinces have likely been quasi-stable for hundreds of millions, perhaps billions of years, and plume heads rise through the mantle in about 30 Myr or less. LIPs provide a direct link between the deep Earth and the atmosphere but environmental consequences depend on both their volumes and the composition of the crustal rocks they are emplaced through. LIP activity can alter the plate tectonic setting by creating and modifying plate boundaries and hence changing the paleogeography and its long-term forcing on climate. Extensive blankets of LIP-lava on the Earth's surface can also enhance silicate weathering and potentially lead to CO_2 drawdown (cooling), but we find no clear relationship between LIPs and post-emplacement variation in atmospheric CO_2 proxies on very long (>10 Myrs) time-scales.

Subduction is a key driving force behind plate tectonics but also a key driver for the long-term climate evolution through arc volcanism and degassing of CO_2. Subduction fluxes derived from full-plate models provide a powerful way of estimating plate tectonic CO_2 degassing (sourcing) and correlate well with zircon age frequency distributions through time. This suggest that continental arc activity may have played an important role in regulating long-term climate change (greenhouse *vs.* icehouse conditions) but only the Permo-Carboniferous icehouse (~330-275 Ma) show a clear correlation with the zircon record.

1. Introduction

The Earth's surface is ever changing as a reflection of how the deep Earth interacts with its crust and atmosphere. By controlling the distribution of continents and oceans, construction of mountains, arc-volcanism, topography and weathering, the process of plate tectonics plays an intricate role in shaping the climate on geological time-scales. On shorter time-scales, Large Igneous Provinces (LIPs) can directly perturb the climate system through the massive release of gases to the atmosphere (Fig. 1a), either from lavas and shallow intrusions, or remobilized

from sedimentary rocks subjected to metamorphism in contact with sub-volcanic sills, dykes, and igneous centres (Svensen *et al.* 2004). LIPs mark punctuated periods in Earth's history characterized by an initial onset phase followed by a large volume flux ('acme'; generally over geologically short timescales), and a waning phase (e.g. Jerram & Widdowson 2005). This main acme phase which sees the largest volumes of melt emplaced/erupted is often about one million years (Myr) or shorter in duration (e.g. Ernst 2014). Such short-lived events have had a profound influence on the shaping of the Earth's surface and directly contribute to the Earth's atmosphere and biosphere. Therefore, a causal link between LIPs and mass extinctions has long been postulated (e.g. Wignall 2001). The LIPs themselves are manifest on the Earth's surface in the form of giant 'Traps', i.e., lava sequences, sill and dyke complexes, and large igneous centres, with preservation dependant on age, style of emplacement and erosional/tectonic circumstances (field examples of preserved parts of various LIPs through time are shown in Fig. 2). The rapid reshaping of the Earth's surface with aerially extensive blankets of lava can lead to large areas of juvenile volcanics undergoing weathering and erosion, thereby contributing to the sedimentary budget (Jones *et al.* 2016).

In the case of lava and magma degassing, the volatiles are ultimately sourced from the mantle and include carbon dioxide (CO_2), sulphur dioxide (SO_2), and hydrogen chloride (HCl). The emplacement of melts into sedimentary basins (Fig. 1a) generates additional volatiles during prograde heating of the surrounding sedimentary rocks. Such reactions involve the release of methane (CH_4), CO_2, SO_2, HCl, and halocarbons from vast, volatile-rich reservoirs such as shale, coal, carbonates, and evaporites. Depending on the melt fluxes during the evolution of LIPs, the released gases may cause a range of environmental and climatic effects on various timescales (e.g. Jones *et al.* 2016). Aerosol-generating SO_2 may trigger initial global cooling on very short time-scales (years), CH_4 and CO_2 can lead to global warming over longer time-scales (10^2–10^5 years), whereas HCl and halocarbons perturb the atmospheric chemistry and can destabilize the ozone layer (Svensen *et al.* 2009; Black *et al.* 2012). The large volume of magma input into the Earth's surface system also leads to a marked increase in mercury (Hg) released into the environment, eventually deposited in sedimentary archives (e.g. Sanei *et al.* 2012). High-resolution stratigraphic studies and new proxies (such as Hg) have strengthened the view that LIPs may have played an important role in triggering key events such as mass extinctions and oceanic anoxia through rapid climate perturbations. Examples include the end-Permian (~252 Ma; Siberian Traps) and end-Triassic events (~201 Ma; Central Atlantic Magmatic Province, CAMP), the Early Toarcian (~183 Ma; Karoo-Ferrar LIP), and the

Paleocene-Eocene Thermal Maximum (North Atlantic Igneous Province, NAIP) at around 56 Ma (Figs. 3b-e).

LIP emplacement (Fig. 4a) highlights a direct link between plume generation processes in the deep mantle (Fig. 1b), dynamic interactions within the Earth's crust, and changes within the atmosphere-hydrosphere-biosphere system. Mantle plumes preferentially rise from the margins of two thermochemical anomalies in the deepest mantle (Burke & Torsvik 2004; Burke *et al.* 2008; Torsvik *et al.* 2006, 2010a, 2014, 2016). These regions (Fig. 4b) are known as large low shear-wave velocity provinces (LLSVPs; Garnero *et al.* 2007, 2016), or simply dubbed TUZO (The Unmoved Zone Of Earth's deep mantle) and JASON (Just As Stable ON the opposite meridian), beneath Africa and the Pacific, respectively (Burke 2011), to honour the pioneering works of Tuzo Wilson (e.g. Wilson 1963) and Jason Morgan (e.g. Morgan 1971).

A simple model of surface-mantle interaction has emerged after the recognition of a remarkable correlation, not only between active hotspot volcanoes and present day deep mantle structures (Fig. 5a), but also reconstructed kimberlites and LIPs (Fig. 4b) for the past 300 Myrs. Numerical models of mantle convection made to investigate the stability of TUZO and JASON have shown that it is possible to maintain stability for hundreds of millions years (Steinberger & Torsvik 2012; Bower *et al.* 2013; Bull *et al.* 2014) and their continued existence for billions of years (Mulyukova *et al.* 2015a). However, the long-term stability of TUZO and JASON with plumes sourced from their margins is debated (e.g., Austermann *et al.* 2014; Davies *et al.* 2015; Zhong *et al.* 2007; Zhang *et al.* 2010; Zhong & Rudolph 2015; Doubrovine *et al.* 2016; Torsvik *et al.* 2016; Hassan *et al.* 2016; Flament *et al.* 2017; Tegner *et al.* 2019), some LIPs may not have been originating from plumes (e.g., Coltice *et al.* 2007), and some question the very existence of mantle plumes (e.g., Julian *et al.* 2015). We therefore briefly review the *observational* evidence for the existence of specific plume generation zones and LLSVP stability (Section 2), before moving on to estimates for how long plumes take to travel from the core-mantle boundary (CMB) to the base of the lithosphere (Section 3). Catastrophic melting at the base of the lithosphere can lead to the formation of LIPs at the surface and consequent atmospheric perturbations that are temporally linked to abrupt climate changes and mass extinctions (Section 4).

The long-term role of LIPs in the Earth system include a reduction in atmospheric CO_2 (cooling) on long time-scales (10^5 to 10^6 years) through enhanced silicate weathering. The chemical weathering of silicates sequesters atmospheric CO_2 by providing alkalinity and dissolved cations (Ca, Mg) to the oceans, which promotes carbonate formation (Walker *et al.* 1981). Moreover, the supply of nutrients and reactive Fe causes the enhanced burial of organic

carbon (Hawley *et al.* 2017). Combined, these effects work to lower atmospheric CO_2 on a range of timescales from seasonally (organic carbon) to >10,000 years (carbonate formation). The denudation of basaltic terrains is a particularly important component of silicate weathering, with modern estimates predicting that such terrains contribute 30-35 % of the terrestrial silicate flux, despite comprising only ~5 % of the continental surface area (Dessert *et al.* 2003). Projected subaerial extents of LIPs are a similar order of magnitude to the modern aerial extent of basaltic terrains (6.85 x 10^6 km^2), indicating that the arrival of abundant lavas and volcanic products at the Earth surface may have a strong impact on global silicate weathering rates.

Weathering is largely controlled by relief and climate, where LIPs in cold and dry climates weather slowly, and warm and wet environments lead to rapid weathering. A striking example is the difference between the CAMP emplaced at 201 Ma and the Siberian Traps erupted at 252 Ma. The CAMP (Fig. 2f) was emplaced in the tropics (Fig. 3d) and most of the flood basalts are argued to have eroded rapidly (Marzoli *et al.* 2018), which makes it very challenging to reconstruct the original LIP volumes, including melt fluxes and volatile release (Svensen *et al.* 2018). The present day volume of the CAMP *flood basalts* is estimated to be about 0.1 x 10^6 km^3, and with an original volume on the order of 1.5 x 10^6 km^3; this represents a preservation of ~7% (cf. Marzoli *et al.* 2018). In contrast, the Siberian Traps, located at ~60° North (Fig. 3d) since the Triassic, still have about 22% of the original flood basalt volume remaining (cf. Vasiliev *et al.* 2000; 0.651 x 10^6 km^3 of present day flood basalts versus an assumed original volume of 3 x 10^6 km^3). Although the original volume of the Siberian Traps flood basalts is poorly constrained, it would need to be 8.6 x 10^6 km^3 in order to obtain the same percentage of preservation as that for the CAMP. In section 5 we consider such long-term effects stemming from the complex interplay of LIP emplacement, paleogeography, weathering, atmospheric CO_2 fluctuations and climate.

2. Observed links between deep Earth and surface volcanism

There are three distinct kinds of volcanic systems that are interpreted to be related to the deep mantle: LIPs (Fig. 4b), kimberlites, and hotspot volcanoes (Fig. 5a). Almost all of these features laid, at the time of their original eruption, vertically or nearly vertically above the margins of TUZO and JASON. By comparing restored LIPs with global tomographic shear-wave models (Torsvik *et al.* 2006; Doubrovine *et al.* 2016), it becomes apparent that most reconstructed LIPs overlie a contour of constant velocity which corresponds to the largest horizontal velocity gradient in the lowermost mantle. That is the 1% slow contour in the *smean* model (Becker & Boschi 2002), or the 0.9% slow contour in the *s10mean* model (Doubrovine *et al*. 2016), both

at 2800 km depth. This contour was originally dubbed the faster/slower boundary (Torsvik *et al.* 2006) and later the plume generation zone (PGZ; Burke *et al.* 2008; red lines in Figs. 4b, 5). Global shear-wave-velocity models provide broadly similar characteristics near the CMB (e.g., Torsvik *et al.* 2008a, 2014; Doubrovine *et al.* 2016; Garnero *et al.* 2016), the choice of tomographic model is therefore not critical to our analysis below, but leads to slightly different statistical correlations. Also note that *smean* (Becker & Boschi 2002) and *s10mean* (Doubrovine *et al*. 2016) are averaged from three and ten global shear-wave-velocity models, respectively. Around 30 global tomography models can be visualized and compared at http://submachine.earth.ox.ac.uk (Hosseni *et al.* 2018).

Hotspots are commonly referred to as volcanism unrelated to plate boundaries and some define linear chains of seamounts and volcanoes with a clear age progression (e.g. the Hawaiian Chain). A few hotspots also lie at the ends of volcano chains connected to a starting LIP, e.g., the Tristan (Paraná–Etendeka) and Réunion (Deccan) hotspots, whilst the New England hotspot (Doubrovine *et al.* 2012) lies at the end of a trail that was connected with Jurassic kimberlite volcanism in continental North–East America (e.g. Zurevinski *et al.* 2011). Numerous catalogues of hotspots have been compiled and published (e.g. Richards *et al.* 1988; Sleep 1990; Steinberger 2000, Courtillot *et al.* 2003; Torsvik *et al.* 2006; Morgan & Morgan 2007), but many hotspots in these lists may not have a deep plume origin. Consequently, we here only analyse 27 hotspots (Fig. 5a, Table 1) classified as being sourced by deep-rooted plumes from seismic tomography (French & Romanowicz 2015). Most are today located near-vertically above the margins of TUZO and JASON and plot on average $5.9 \pm 4.4°$ (great-circle distance, the shortest distance on a sphere, and reported with standard deviation) from the PGZ (0.9% slow contour in the *s10mean* model). Eruptions of kimberlites (ultrabasic magmas) were exceptionally rare in the past 50 Myrs (Fig. 3f; Torsvik *et al.* 2010a), but the youngest known kimberlite volcanoes ─ the Igwisi Hills volcanoes in Tanzania (Dawson 1994) ─ erupted near-vertically above the eastern margin of TUZO (Fig. 5a) at around 12,000 years ago (Brown *et al*. 2012). This young kimberlite and all hotspots in the Indo-Atlantic realm are located directly above the margins of TUZO whilst a few of the deeply sourced Pacific hotspots (e.g. Tahiti) are displaced toward the interior of JASON (Torsvik *et al.* 2016).

In contrast to hotspots, LIPs (Fig. 4a, Table 2) and kimberlites (except the young Igwisi Hills) must be reconstructed in a mantle reference frame in order to explore their links to present day deep-Earth mantle structures. Fig. 4b summarizes our latest reconstructions of 32 Phanerozoic LIPs between 510 and 15 Ma. We use a global moving hotspot reference frame back to 83.5 Ma which has been extended by a separate Indo-Atlantic moving hotspot reference

frame back to 120 Ma (Doubrovine *et al.* 2012) and ─ except for the young and relatively small Colombia River Basalt ─ the restored LIPs fall near-vertically above the plume generation zones of an assumed fixed TUZO (5.0 ± 2.7°, N=10 LIPs, red coloured squared symbols in Fig. 4b). About 80% of all kimberlites that occurred since Pangea formed (Torsvik *et al.* 2010a) show a close link to the margins of TUZO ─ and as an example ─ reconstructed kimberlites from southern Africa (South Africa, Botswana, Angola and Lesotho) with ages between 80-90 Ma and 110-120 Ma (dominating the two peaks in global kimberlite occurrences; Fig. 3f) plot 12.8 ± 1.0° (N=451 kimberlites) from the PGZ (white coloured squared symbols in Fig. 4b).

The Pacific Plate can only be linked through plate-circuits to the Indo-Atlantic realm for the last 83.5 Ma, and before that, the Pacific Plate must be referenced directly to the mantle using a fixed hotspot scheme. Here we use a new hotspot model of Torsvik *et al.* (2019) to reconstruct Pacific LIPs between 100 Ma (Hess Rise) and 144 Ma (Shatsky Rise). The new model show similarities to that of Wessel and Kroenke (2008) but net lithosphere rotation and Pacific Plate velocities are much lower, and a total of six reconstructed Pacific LIPs (yellow squared symbols in Fig. 4b) fall near-vertically above the PGZ of JASON (3.2 ± 2.8°, N=6 LIPs). No kimberlites are related to JASON for the past 320 Ma since kimberlites are mostly derived from great depths in continental lithosphere and no continents have overlain JASON since Pangea formed. In the Indo-Atlantic domain, LIPs older than 120 Ma are reconstructed with true polar wander (TPW) corrected paleomagnetic data (Torsvik *et al.* 2012; Doubrovine *et al.* 2016; Torsvik 2018), and reconstructed LIPs between 120 Ma and 297 Ma (Fig. 4b) also closely correlate with the PGZs of TUZO (4.1 ± 3.1°, N=11 LIPs). This is also the case for most kimberlites before 120 Ma, and as an example, reconstructed North American kimberlites (USA, Canada) with ages between 120 and 300 Ma cluster along the northwest PGZ margin of TUZO (4 ± 4°, N=181 kimberlites; grey coloured squared symbols in Fig. 4b).

Austermann *et al.* (2014) and Davies *et al.* (2015) have argued that the observed correlation between the reconstructed LIPs and the margins of TUZO and JASON (Fig. 4b) can be equally well or even better explained by deep plumes forming randomly over the entire area associated with the LLSVPs. This criticism was addressed statistically in Doubrovine *et al.* (2016), and although the hypothesis proposing that LIP-sourcing plumes form randomly over the entire area of TUZO and JASON cannot be ruled out, probability models assuming plumes rising from their margins provide a much better fit to the observed distribution of reconstructed LIPs.

The striking spatial correlation between reconstructed LIPs and the PGZs of TUZO and JASON for the past 300 Ma (also the case for kimberlites and TUZO PGZs) implies that TUZO

and JASON have remained quasi-stable since Pangea formed. Taking a step further, if we assume that TUZO and JASON were likewise stable in earlier time (before 300 Ma), we can calibrate continental longitudes in such a way that LIPs and kimberlites erupted above the edges of TUZO and JASON (Torsvik *et al.* 2014). This is known as the plume generation zone reconstruction method and there are ~300 kimberlites but only three Paleozoic LIPs to be reconstructed in this manner, i.e. the ~360 Ma Yakutsk LIP (Siberia), the ~400 Ma Altay-Sayan LIP (South Siberia) and the ~510 Ma Kalkarindji LIP in Western Australia. All three of these LIPs erupted in the northern hemisphere (Fig. 3d), and in a mantle frame (i.e. corrected for TPW) *modelled* to be sourced by plumes from the northeast margin of TUZO (green triangles in Fig. 4b). We have also restored a younger LIP, the ~260 Ma Emeishan LIP, to the western margin of JASON using this method (Fig. 4b). The longitude of South China is otherwise unknown as it cannot be tied to the Indo-Atlantic reference frame through plate circuits because it was not an integrated part of Pangea in the Late Paleozoic (Torsvik *et al.* 2008a; 2014; Jerram *et al.* 2016a; Torsvik & Domeier 2017).

There is also a High Arctic LIP (HALIP), originally considered to include only Upper Cretaceous volcanics, on Axel Heiberg Island in the Canadian Arctic (Tarduno *et al.* 1998), but extended to be grouped with magmatism in many other places in the High Arctic (e.g., Svalbard, Franz Josef Land and the Barents Sea). Because radiometric ages for HALIP show a wide range (130-80 Ma) and a plume centre is not readily defined, HALIP is not shown in our reconstructions of LIPs (Fig. 4b). However, assuming that peak activity occurred around 124 Ma (based on U/Pb data on sills; Corfu *et al.* 2013) and a tentative plume centre just to the north of Ellesmere, we estimate an eruption latitude of ~60°N (paleomagnetic frame; Fig. 3d, Table 2) ─ and sourced by a mantle plume from the northernmost areas of TUZO. The Cretaceous Caribbean LIP is also not included in our analysis (Fig. 4b) because of plate reconstruction uncertainties and an unknown plume centre. But using an age of ~90 Ma and a tentative plume centre near the western margin of central Americas we estimate an eruption latitude near the Equator (Fig. 3d, Table 2), and sourced by a plume from the eastern margin of TUZO.

3. Plume ascent scenarios

Over the past decade considerable effort has been dedicated to estimating the sinking rate of subducted slabs through the lower mantle. On a global scale, van der Meer *et al.* (2010) determined an average lower-mantle slab sinking rate of ~1.2 cm/yr., but on the basis of a larger subduction dataset this sinking rate was later refined and determined to be non-linear (van der Meer *et al.* 2018). Interpretation of lower mantle slab ages critically depend on their upper

mantle history (Fig. 6a): some slabs may directly penetrate the base of the transition zone (660 km), whilst others flatten and may stagnate for tens of million years (e.g. Goes *et al.* 2017). Nevertheless, a first-order estimate of whole mantle slab sinking rates will prove useful for our purposes here. Assuming sinking rates in the upper mantle of ~5 cm/yr, possible delays in the transition zone, and 1-2 cm/yr sinking rates in the lower mantle (van der Meer *et al.* 2010, 2018; Domeier *et al.* 2016), the estimated time for slabs to reach the lowermost mantle above the core-mantle boundary (CMB) is about 200-240 Myrs (Fig. 6a). This is approximately twice as long as predictions derived from geodynamic models (Steinberger *et al.* 2012) although some convection models show such timing when viscosity increases with depth and thermal expansivity decreases too (Cízková *et al.* 2012).

Subducting slabs impose global flow, which influences the formation of instabilities and mantle plumes along the margins of TUZO and JASON (Figs. 1b, 6a). As sinking slabs approach the CMB, they push material, including the hot thermal boundary layer above the CMB, ahead of them. Once these hot, displaced materials reach the boundary with the hot, but chemically dense LLSVPs, they are forced upward, and may start to rise in the form of plumes (Steinberger & Torsvik 2012). We therefore have a consistent picture of how and where plumes may start their protracted journey from the deep Earth ─ but a key question is how long does a plume take to travel from the CMB to the base of the lithosphere? This could be estimated analytically for a Stokes sphere, and numerical model results also exist (e.g. Lin & Van Keken 2006), but these results are unreliable, due to large uncertainties, especially in mantle rheology and the composition of plume material. Here we therefore take an alternative approach and investigate this question by finding plume ascent times from source locations in the lowermost mantle that most closely coincide with the edges of the LLSVPs, following the assumption that their margins should act as PGZs.

Plume source locations are determined by using an extension of an existing method: Steinberger & O'Connell (1998) initiated their computation with a vertical conduit at the time of plume head eruption. This approximation corresponds to a plume head that rises very fast, such that the conduit, which trails the head, is not much distorted during ascent of the head. They computed how, subsequent to eruption of the plume head, the conduit gets distorted and the surface hotspot moves accordingly. Here we extend this computation by taking a finite ascent time of the plume head into account, during which the motion and distortion of the conduit is already considered. Our aim then, is to determine an ascent time that will restore a plume from its present-day surface location (which we know) to an original source location in the lowermost mantle that is proximal to a PGZ. We make the simplifying assumption that

plume head rising speed is inversely proportional to ambient mantle viscosity at that depth, and absolute values are chosen such that a specified total ascent time results. Because viscosity reaches its maximum in the lower part of the lower mantle, plume heads rise most slowly in that depth range, and their lateral advection is therefore dominated by the horizontal flow component at those depths. In general, because that flow is dominated by a degree-2 pattern with horizontal flow converging towards the two LLSVPs (Fig. 6a), the rate at which a plume ascends controls the computed location of its source and specifically its distance from a PGZ: the slower a plume ascends, the farther its original source location must lie from the edge of the nearest LLSVP. The question to be addressed hence is whether there is a single ascent time, or a range of times, for which the computed plume source locations match the PGZs comparatively well? This could then be seen as an indication for the realistic time it takes a plume to rise. Obviously, one simplification of this approach is the assumption that, for a given model case, all plumes take the same time to rise through the mantle. *In reality plume heads may have different sizes and hence rise at different speeds through the mantle*. Furthermore, a plume head may ascend faster or slower because of rising or sinking ambient mantle flow. A second implicit assumption of this approach is that all plumes should have nucleated along a PGZ (see Appendix 1 for method details).

Figure 5b shows the computed plume head source locations in the lowermost mantle. Present-day hotspot locations (Fig. 5a) tend to be near the surface-projected PGZs, but occur both inside (over the LLSVP) and outside the boundary itself. Our computed hotspot surface positions through time, in the case with initially vertical plume conduits (Steinberger & O'Connell 1998; Steinberger 2000; Steinberger *et al.* 2004), tend to remain near the margins, as there is no clear trend, in this case, whether the hotspot moves towards, or away from the LLSVPs. This is because the advection of the plume conduit, and hence the hotspot surface motion is influenced by both flow in the upper half of the mantle, which tends to be *away from* LLSVPs and the lower half *towards* LLSVPs. As the initially vertical plume conduits get distorted, the hotspot position initially tends to move with upper-mantle flow. Later on, segments of the tilted conduit buoyantly rise to the surface and thus the motion of older plumes rather tends to be in the direction of lower mantle flow. This is also the case for flow that is not time-dependent, i.e. it is not necessary to have time-dependent flow in order to obtain time-dependent hotspot motion. Hence for younger plumes the motion away from LLSVPs tends to dominate and for older ones the motions towards, but because of compensating effects the overall hotspot motion is rather slow – leading to the concept of fixed hotspots (Morgan 1971) – and the total amount of motion is rather small and not preferentially directed towards or away

from the LLSVPs. Hence the modelled initial plume positions required to match present-day hotspot positions, and the initial plume source locations, which in this case are vertically below (red squares in Fig. 5b), are near the margins at a similar average distance to the PGZs as present-day hotspots.

Because flow in the lowermost mantle is directed towards the LLSVPs, a finite plume head rise time will be associated with a trade-off between that ascent time and the distance between the plume's source location and an LLSVP margin. The longer a plume head takes to rise to the surface, the further away from the LLSVP margins (and also from their interiors) it must have started in the lowermost mantle in order to reach the surface location observed at present day (near the projected PGZs). This clear trend can be seen both in Fig. 5b and in Fig. 6b, which also shows that this trend holds for two tested tomography models, and regardless of whether time-dependence of flow, and the thermochemical excess density of LLSVPs is considered (see Appendix 1). It also shows that the slope of the mean distance *vs.* rise time curve generally gets steeper with increasing rise time. That is, increasing the rise time e.g. from 0 to 30 Myr has less of an effect – the predicted plume source locations tend to remain near the LLSVP margins – than increasing the rise time from e.g. 60 to 90 Myr (Fig. 6b). Backward-advection of density anomalies leads to increasing stratification of the density field back in time, leading to decreasing flow velocities. Therefore, the average distance increases less strongly with plume head rise time in this case; however, the stronger increase without backward-advection (black and brown lines in Fig. 6b) may actually be more appropriate. The observed trend, though, holds independent of the uncertain backward-advection. Also, disregarding thermochemical excess densities in LLSVPs corresponds to stronger density anomalies causing stronger flow, hence a stronger dependence of average distance on plume head rise time (violet and blue lines in Fig 6b). Another reason that speaks against slow rising of plume heads is that for rise times of ~80 Myr and more, an increasing number of cases occurs where the present-day hotspot position cannot be matched – which also slightly affects the results shown in Fig. 6b.

Our approach favours that plume heads rise through the mantle in ~30 Myr or less ─ rather fast compared to what could be inferred from simple geodynamic considerations: Using Stokes' formula and a density contrast of 30 kg/m^3, which corresponds to realistic values of temperature and thermal expansivity for a thermal plume *vs.* the surrounding mantle (Steinberger & Antretter 2006), a plume rise time of 60 Myr corresponds to a plume head with a very large diameter of ~1600 km. The head radius inferred from Stokes' formula is inversely proportional to the square root of rise time; hence a more realistic diameter of 1000 km

(Campbell 2007) would correspond to a rise time of more than 150 Myrs, which is incompatible with our results. There are several ways to resolve this apparent discrepancy: Firstly, plume heads could be much larger than often assumed, although this would imply much lower melting rates than commonly assumed to explain the volume of flood basalts (Richards *et al.* 1989), or that melting only occurs in a small part of the plume head. Second, it is plausible that plume heads encounter a lower-than-average ambient mantle viscosity, as they rise through the mantle above the LLSVPs, where the mantle may on average be hotter, and hence less viscous. They may also be aided by large-scale flow which tends to be upward above the LLSVPs (Conrad *et al.* 2013). In addition, if viscosity is stress-dependent, effective mantle viscosity may be reduced in the surroundings of the plume head, further reducing rise times. The inferred rather fast plume ascent speeds contrasts with the sinking of slabs, which appear to sink (van der Meer *et al.* 2010, 2018; Domeier *et al.* 2016) only about half as fast as geodynamic models would predict.

Combining plume ascent times of ~30 Myr and slab sinking times ~200 Myr with the time that basaltic material remains near the CMB (also ~30 Myr, if we assume an average horizontal flow speed of ~10 cm/yr, and a typical distance from where slabs reach the lowermost mantle to the PGZs of about 3000 km), we estimate that ~260 Myr must elapse from the subduction of oceanic crustal materials until eruption of recycled crustal components in hotspot lavas, whereby the most time is spent on the way down. This time could be much longer, if basaltic materials get first incorporated into the thermochemical piles (Fig. 6a), before they become entrained into plumes. Numerical models of Mulyukova *et al.* (2015b) show that a large fraction of basaltic material is effectively immediately recycled, entrained by plumes, i.e. the age versus frequency of occurrence plot tends to show a maximum at a young age, but there is also a long tail towards older ages, i.e. material can linger near the CMB for a billion years and longer, and there is considerable variability in the age distribution between individual plumes. In contrast, the time from when a slab starts sinking (i.e. a new subduction zone is formed) until a plume rises to the surface in response to the sinking of that slab can also be considerably shorter than the ~260 Myrs estimated for material transport – perhaps only about half as long – as the slab pushes material ahead it and therefore influence the formation of instabilities and plumes long before it has even reached the lowermost mantle (Steinberger & Torsvik 2012).

4. Volcanism and environmental effects on various timescales

We estimate that plumes rise through the mantle in ~30 Myr or less and the surface manifestations are hotspots, kimberlites, and LIPs. In terms of environmental effects, hotspot and subduction related volcanoes can be significant sources of climate-sensitive gases such as

halogens, carbon and sulphur species that can disturb the climate on a wide range of timescales (Jones *et al.* 2016). While stochastic in nature, global volcanism is fairly constant on a millennial timescale. Large individual eruptions can lead to climate disturbances such as a sulphate aerosol cloud inducing a net cooling of the Earth's surface (e.g., Robock 2000; Thordarson *et al.* 2001; Thompson *et al.* 2009, Toohey *et al.* 2016), but these impacts are temporally restricted to a few years and are therefore limited as a long-term climate forcing (Schmidt *et al.* 2012). The radiative effects of volcanic aerosols produced by short-lived explosive hotspot and kimberlite volcanoes generally have relatively small climate effects compared with that of LIPs due to the volumetric and flux differences. In order to further discuss the environmental effects of plume-related volcanism, we start by addressing kimberlite eruptions before moving on to LIPs.

4.1 Kimberlites

Hotspot observations are known from present day examples (e.g. from Hawaii and Iceland) whereas kimberlites eruptions have not been witnessed in modern times. It can be shown that the majority of Late Paleozoic-Recent kimberlites are related to TUZO (Torsvik *et al.* 2010a), and clearly linked with the mantle as they are derived from great depths (>150 km; Wyllie 1980; Mitchell 1986), entraining host rocks from the mantle upwards during rapid ascent as witnessed by the fragmental content of the erupted products (e.g. Jerram *et al.* 2009). Around 75% of all known Mesozoic-Cenozoic kimberlites are of Cretaceous age (~1100 known pipes), and they have intruded many cratonic areas (North America, Brazil, Australia, East Antarctica and India) — but the vast majority of these (~77%) intruded the Kalahari and Congo cratons in southern Africa at intermediate southerly latitudes (e.g., Fig. 7a, b).

Kimberlite magmas are almost exclusively associated with old cratons and the ascent of kimberlites is considered to be anomalously fast even though they carry substantial mantle-derived payloads, i.e. xenoliths and xenocrysts (including diamonds). The exsolution of dissolved volatiles (primarily CO_2 and H_2O) is considered essential for providing adequate buoyancy for the high ascent rates of dense crystal-rich magmas as well as the cone-like kimberlite shape caused by explosive eruptions (Russel *et al.* 2012). Kimberlites provide direct conduits between the deep mantle and the atmosphere. Kimberlite magmas with very high carbonate contents (CO_2 ~20 wt. %) are estimated to rise to the surface in a matter of hours from great depths, and eruption durations are probably on the order of weeks and substantial volumes of CO_2 can therefore be released at high rates (Patterson & Don Francis 2013).

Oceanic anoxic events (OAEs) witness short interludes (< 1 Myrs) where parts of the seas were markedly exhausted in oxygen (e.g. Jenkyns 2010), and these are often viewed as the Earth's response to the injection of huge volumes of CO_2 into the atmosphere and hydrosphere (e.g., Percival *et al.* 2015). LIP volcanism has been linked to several OAEs (Section 4.2) but peak Phanerozoic kimberlite activity during the Cretaceous (Fig. 3c,f) clearly overlaps with OAE1 (~121 Ma and ~111 Ma) and OAE2 (~94 Ma), and at times with limited continental LIP activity (Fig. 7c). At least 850 kimberlites with ages between 80 and 130 Ma are known. Some kimberlite ages are based on Rb-Sr and K-Ar methods, and some are not directly dated but inferred from neighbouring kimberlite ages; if we only analyse kimberlites dated by U/Pb (zircon/perovskite) between 80 and 125 Ma, we notice clear age peaks that overlap with OAE1 and OAE2 (Fig. 7c). The largest concentration of kimberlites in Earth history — mostly in southern Africa and erupted at intermediate southerly latitudes (Fig. 7a,b) — is therefore temporally coincident with Cretaceous OAEs. The role of kimberlites in triggering OAEs is uncertain as kimberlites are restricted in volume and occurrence but the eruption of large kimberlite clusters could potentially deliver enough CO_2 to the atmosphere to trigger sudden global warming events. Patterson & Don Francis (2013), for example, have estimated that a kimberlite cluster of ~50 pipes could produce about 1000 Gt of carbon in a few years.

4.2 Large igneous provinces and global changes

Continental LIPs are generally defined as predominantly mafic volcanic provinces that were emplaced in a short time period (1-5 Myr) covering at least 100,000 km^2 with a volume of more than 100,000 km^3 (Ernst 2014). They are often characterized by extensive flood basalt sequences commonly termed 'Traps' (Svensen *et al.* 2019) comprising thick lava sequences (Self *et al.* 1998), by explosive/fragmented volcanic deposits (both from mafic and silicic eruptions; e.g. Bryan *et al.* 2002), and by sheet-like or plutonic intrusions in sedimentary basins and other crustal settings (e.g. Jerram *et al.* 2010; Svensen *et al.* 2018; see examples in Fig. 2). Clearly such events, driven by upwelling from the mantle below, have impacts on the topography at a regional to continental scale, and on the biosphere and atmosphere, not only due to the sheer volume of igneous material added to the crust, but due to volcanic and metamorphic degassing (Fig. 1a) during the LIP evolution.

The potential environmental impact of any LIP is governed by numerous processes, chief among them: the amounts and degree of magmatic degassing, the composition of the crust heated by the igneous plumbing system and the fate of subsequent metamorphic generated gases (crustal storage *vs* seepage *vs* rapid venting to the atmosphere), the particular state of the climate

and tectonic configurations at the time of LIP formation, and the paleolatitude of the emplacement. LIPs themselves can be rather mixed in terms of the relative volumes of intrusions *vs* lava flows *vs* explosive eruptive products (Bryan *et al.* 2010; Jerram *et al.* 2016b). This is why the climatic response to LIP emplacement must have varied through the geological record, with no clear correlation between the estimated volume of a LIP and the severity of the related environmental disturbance (e.g., Wignall 2001; Jones *et al.* 2016) (Fig. 3b-e). Volume estimates and rates of LIP emplacement are also challenging to derive due to few field-based volume estimates of individual flows or sills, buried/offshore parts of LIPs (Fig. 8a) being inaccessible or poorly known, and due to geochronological limitations. Recent estimates from the Karoo-Ferrar LIP, for example, suggest emplacement rates of 0.78 km^3/y, calculated from the present-day sill volume assuming a steady state emplacement over 0.47 Myr (derived using U-Pb zircon ages and Monte Carlo age modelling; Svensen *et al.* 2012). Other Karoo-Ferrar LIP estimates are based on melt extraction rates from the mantle during a 6 Myr period, giving results of 0.3 km^3/y (Jourdan *et al.* 2005).

There are five big Phanerozoic mass extinctions: The first one (end-Ordovician) is not linked to any known LIP (Fig. 3b-e), but three of the big five have been linked to LIP emplacement; i.e. the Yakutsk-Vilyui LIP (Devonian Extinction), the Siberian Traps (End-Permian, Fig. 2g) located in the Siberian Craton and the Central Atlantic (CAMP - Triassic-Jurassic Extinction, Fig. 2f). The fifth mass extinction (Cretaceous-Tertiary Extinction) has also been linked to a LIP in India (Deccan Traps, Fig 2c), as highlighted in Fig. 3 and Table 2, but it was likely the combination of the toxicity caused by the Deccan Traps and the effects of an asteroid together that were responsible for the mass extinction (Alvarez et al. 1980). Moreover, LIPs coincide in time with climate change and several OAEs (Fig. 3c-d), an observation for which numerous authors have assigned a causal relationship. Examples include the Toarcian event (linked to the Karoo-Ferrar LIP) and the Paleocene-Eocene Thermal Maximum (PETM) linked to the Northeast Atlantic Igneous Province (Svensen et al. 2004; Jones *et al.* 2019; Fig. 8a,b). PETM is associated with global disturbances in carbon isotopes and dissolution of $CaCO_3$ sediments. The origin of the PETM at around 56 Ma is still debated and in addition to the proposed link to volcanic activity in the northeast Atlantic, explanations for the PETM include methane hydrate dissociation (Dickens *et al.* 1995), comet impact (Kent 2003), global wild fires (Kurz *et al.* 2003) or kimberlite eruptions in Canada (Patterson & Francis 2013).

LIPs release massive volumes of greenhouse gases quickly to the atmosphere. These can be in the form of direct volcanic degassing and from gases escaping from intrusions and their contact metamorphosed host rocks (e.g., Svensen *et al.* 2004, 2009; Heimdal *et al.* 2018;

Ganino & Arndt 2009; Jones *et al.* 2016). Such rapid degassing can explain how LIPs can trigger global climate change and mass extinctions (Vogt 1972; Courtillot & Renne 2003; Wignall 2001; Bond & Wignall, 2014; Fig. 3b-d). Voluminous degassing from magmatic and organic-rich metamorphic sources alone could be in excess of 30,000 Gt CO_2 for LIPs such as the Siberian Traps (Beerling *et al.* 2007; Courtillot & Renne 2003; Sobolev *et al.* 2011; Svensen *et al*. 2009) and 80,000 Gt CO_2 for the CAMP (Heimdal *et al.* 2018), which, combined with other associated volcanic emissions, would be sufficient to cause sustained global warming on the order of >100,000 years. The eruption of halogens and halocarbons, in particular HCl, HF, and CH_3Cl, are predicted to cause widespread ozone depletion and acid rain, damaging global ecosystems (Visscher *et al.* 2004; Svensen *et al.* 2009; Black *et al.* 2012). LIP eruptions may also emit considerable SO_2, leading to 'volcanic winters' that remain while volcanism is ongoing (Rampino *et al.* 1988).

In the case of LIPs that rise beneath oceanic crust and form submarine basaltic plateaus, the amount of degassing is more limited. They are limited in terms of the production of volatiles through contact metamorphism and/or crustal contamination, and volcanic degassing can be inhibited due to the depth of emplacement. Silicate weathering of LIP products is diminished due to a lack of subaerial exposure, limiting interactions to hydrothermal processes. As such, the environmental impacts of oceanic LIPs appear to be more restricted and less severe than their continental counterparts. Examples of oceanic LIPs include the Ontong Java, Manihiki and Hikurangi Plateaus (Fig. 4a), which have been considered as a single vast and voluminous LIP (~50 x 10^6 km^3) ─ the Ontong Java Nui (Taylor 2006) ─ which erupted at ~123 Ma.

5. LIPs and paleogeography: Long-term effects

On geological time-scales atmospheric CO_2 is mainly controlled by plate tectonic forcing, both via *sources* (volcanic emissions and metamorphic decarbonation in continental arcs) and *sinks* (silicate weathering and organic and inorganic carbon burial) (Walker *et al.* 1981; Berner *et al.* 1983; Marshall *et al.* 1988; Worsley & Kidder 1991; Bluth & Kump 1991; Otto-Bliesner 1995; Raymo *et al.* 1988; Gibbs *et al.* 1999; Berner 2004; Nardin *et al.* 2011; Goddéris *et al.* 2012, 2014). The long-term role of LIP generation is two-fold. Firstly, it includes a reduction in atmospheric CO_2 on long time-scales through enhanced silicate weathering. Second, LIPs punctuate plate tectonics by creating new plate boundaries, thereby changing paleogeography and plate kinematics, and thus plate tectonic forcing.

Silicate weathering can be affected by the rate of erosion of material and the chemistry of the substrate. LIP emplacements can have a large impact on silicate weathering as many of

the constituent minerals that comprise basalt are inherently unstable in hydrous, oxygen-rich conditions. For example, basaltic material is an order of magnitude more weatherable than granitic material (Dessert *et al.* 2003; Gaillardet *et al.* 1999). Therefore, the extrusion of continental flood basalts would provide a significant increase in fresh, weatherable substrate that can then consume atmospheric CO_2 through silicate weathering and related carbon burial. Erosion rates are intrinsically linked to topography, with juvenile and mountainous regions contributing a disproportionately high dissolved and suspended fluvial flux compared to their surface area (Milliman & Farnsworth 2011). If an area affected by a LIP is elevated, either through the emplacement of km-thick flood basalts and/or regional uplift due to thermal buoyancy effects, then the subsequent erosion of that elevated region would considerably enhance atmospheric CO_2 drawdown for thousands to millions of years following its 'uplift' (Jones *et al*. 2016). Erosion is also enhanced by deforestation (applicable since Devonian times), which could be extensive during, and for some time following, the emplacement of a LIP.

Sulphuric acid is also a key component of chemical weathering, as evidenced by numerous modern catchments (e.g. Liu *et al.* 2016; Spence & Telmer 2005). This increases the total weathering of both carbonate and silicate materials, but also replaces some of the weathering done by carbonic acid. This means that if large fluxes of SO_2 are emitted to the atmosphere, then sulphuric acid weathering may either diminish the efficiency of silicate weathering as an atmospheric CO_2 sink, and/or may increase the total weathering of surface silicates. These processes are poorly quantified at present, but are worthy of consideration as the range of volatiles produced by LIP emplacements could have a wide range of both positive and negative feedbacks affecting the long-term carbon cycle.

5.1 Plate tectonic configurations and their modifications by LIPs

The Early Phanerozoic is exceptional because nearly all the continents were located in the southern hemisphere and the latitudinal distribution is readily seen from a "heat-map" (Fig. 9a) which shows how the continental paleolatitude has changed through the Phanerozoic. A key observation to be taken from this heat-map (but also evident from a curve showing the average continental paleolatitude through time; Fig. 9b) is that the continents were effectively restricted to the southern hemisphere during the Early and Middle Paleozoic, but progressively drifted northward in the Late Paleozoic and Early Mesozoic until the break-up of Pangea at ~195 Ma (early Jurassic). From then on, the average paleolatitude of the continents has remained largely stable whilst the latitudinal spread continued to increase substantially (i.e. compare the

latitudinal spread of light areas of the heat-map between times before and after Pangea; Fig. 9a).

The Paleozoic paleogeography was dominated by Gondwana, which amalgamated during Ediacaran-Cambrian times, and stretched from the South Pole to the Equator (Western Australia) during most of the Paleozoic (Fig. 10d). An important ocean (the Iapetus) largely closed during the Ordovician and disappeared entirely during the Silurian (430-420 Ma) when Baltica and Avalonia collided with Laurentia to form Laurussia. Another significant ocean (the Rheic) opened at ~480 Ma (Early Ordovician) between Gondwana and the Avalonia terranes and remained an important ocean until ~320 Ma when Gondwana, Laurussia and intervening terranes collided to form Pangea (Torsvik & Trench 1992; Torsvik & Rehnström 2003; Cocks & Torsvik 2002; Domeier & Torsvik 2014; Domeier 2015; Torsvik & Cocks 2004, 2017). Some tectonic blocks were never attached to Pangea, and thus the term Paleotethys is used for the ocean once separating the China Blocks from Pangea (Fig. 10c). The Panthalassic Ocean (the predecessor of the Pacific Ocean) is best known as the vast ocean that once surrounded the supercontinent Pangea, but 'Panthalassic' also refers to the ocean that dominated more than half the globe (effectively the entire northern hemisphere) in the Early Paleozoic (Fig. 10d).

The distribution of continents and oceans varied immensely before Pangea and its break-up, which mostly occurred along former sutures (Buiter & Torsvik 2014) and was clearly assisted by extensive LIP volcanism. Early Pangea break-up was witnessed by the opening of the Neotethys Ocean (Fig. 11), starting already at ~275 Ma, which was possibly linked to a Tethyan plume that sourced the ~285 Ma Panjal Traps in the western Himalaya (Shellnutt *et al.* 2011) and igneous remnants now preserved in Oman (Arabia). There is an exhaustive list of examples of how LIP activity can change the surface paleogeography by creating and modifying plate boundaries (Torsvik & Cocks 2013; Buiter & Torsvik 2013; Svensen et al. 2018); this as best exemplified among the Atlantic bordering continents: The opening of the Central Atlantic at ~195 Ma (Labails *et al.* 2010; Gaina *et al.* 2013) led to the definite break between North and South Pangea and was preceded by the emplacement of the CAMP (201 Ma; Fig. 11b). The Paraná-Etendeka (134 Ma) heralded the early opening of the South Atlantic (~130 Ma) south of the Walvis ridge (Fig. 7a), and finally, the NAIP assisted the opening of the Northeast Atlantic (~54 Ma). NAIP activity started around 62 Ma (linked to the Iceland plume), and covered vast areas in Baffin Island, Greenland, the United Kingdom, Ireland, the Faroe Islands, and offshore regions, but peak volcanic activity probably occurred at around 56 Ma (coinciding with the PETM event; Fig. 8a,b).

Not all LIPs cause or contribute to changes in plate boundaries (e.g. Kalkarindji, Skagerrak Centred LIP, Siberian Traps; Figs. 10c-d, Fig. 11a), but many conjugate margins are linked to LIPs with break-up occurring almost concurrent with LIP emplacement. In many margins rifting began before the main phase of volcanism, which suggests that rifting was initiated by tectonic forces and that mantle plume material was guided towards the thinned rifted lithosphere to help trigger final continental break-up (Buiter & Torsvik 2013). Continental break-up has fragmented many LIPs shortly after emplacement, with LIP rocks now located on opposed passive margins. Prime examples include CAMP (now mostly located on North America, Northwest Africa and South America; Figs. 4a, 10a,b), Paraná-Etendeka (Brazil and Namibia: Figs. 4a, 7a,b), NAIP (Greenland/North America and Eurasian margin; Fig. 8a), Karoo-Ferrar (South Africa and East Antarctica; Figs. 4a, 7a,b) and Deccan (India and Seychelles). The coastal onshore parts of passive margins may have formed mountainous escarpments of variable height during continental break-up, thus affecting weathering processes. But it is highly disputed whether passive margin uplift is a transient, long-lived, or even permanent phenomenon, as many passive continental margins today (and long after initial break-up) are characterised by elevated plateaux of several kilometres height (e.g., Japsen *et al.* 2011; Osmundsen & Redfield 2011; Redfield & Osmundsen 2012; Steinberger *et al.* 2015).

Plumes impinging the oceanic lithosphere also influence the plate tectonic configuration, e.g. by relocating plate boundaries (ridge jumps) and generating micro-continents, or making entirely new plates such as with the eruption of the ~123 Ma Ontong Java Nui 'mega-LIP' (Ontong Java, Manihiki & Hikurangi Plateaus), which probably led to the break-up of the Phoenix Plate into four new plates at ~120 Ma (Chandler *et al.* 2010; Seton *et al.* 2012; Torsvik *et al.* 2019). The oldest known *in-situ* oceanic LIP is Late Jurassic in age, but most preserved oceanic LIPs were emplaced during the Cretaceous (Fig. 3d; Table 2). The total number of oceanic LIPs will remain unknown as the oceanic crust and the LIPs embedded within it can be recycled back into the Earth's mantle via subduction (e.g. Liu *et al.* 2010; Sigloch & Mihalynuk 2013). Examples of LIPs being recycled today include the ongoing subduction of Ontong Java and Hikurangi Plateau.

5.2 Paleoclimate and atmospheric CO_2

The Phanerozoic was dominated by a greenhouse climate with high atmospheric CO_2 levels (Fig. 12e), interrupted by three main periods of cold (icehouse) conditions, in the End-Ordovician (Hirnantian), Permo-Carboniferous, and the second half of the Cenozoic. Low atmospheric CO_2 is a principal variable in controlling continental-scale glaciations (Royer

2006), but the short-lived Hirnantian cooling event (~445 Ma) is paradoxical because of its apparent association with very high *modelled* atmospheric CO_2 levels. However, the solar luminosity was lower (by 3-5%) and the CO_2 threshold for nucleating ice sheets at that time could have been 4-8 times (1120-2240 ppm) higher than pre-industrial levels of ~280 ppm (Gibbs *et al.* 2000; Herrmann *et al.* 2003; Royer 2006; Lowry *et al.* 2014).

Atmospheric CO_2 concentrations can be estimated from proxies, and the most robust proxies include $\delta^{13}C$ of paleosols, stomatal densities and indices in plants, $\delta^{13}C$ of long-chained alkenones in haptophytic algae, $\delta^{11}B$ of marine carbonate and $\delta^{13}C$ of liverworts (Royer 2006). The averaging of these proxy systems in 10 Myr bins (Fig. 12e) suggests that atmospheric CO_2 values were high between 420 and 400 Ma (~2000 ppm), followed by a pronounced decline to about 500 ppm at ~340 Ma. This shift was probably greatly enhanced by the origin and expansion of forests in the Devonian (Berner 1997) ─ leading to a situation favouring glacial conditions ─ but continental arc-activity and plate tectonic degassing (sourcing) were also reduced during Late Devonian-Carboniferous times (Fig. 12d; Section 5.4). Pangea assembly also culminated with the Alleghenian-Variscan Orogeny, which resulted in a low-latitude (equatorial) orogenic belt of ~7500 km in length across the heart of Pangea (Fig. 11a), and that may also have accelerated weathering and removed more CO_2 out of the atmosphere. It has also been argued that arc-continent collisions contributed to cooling through exhumation and erosion of mafic and ultramafic rocks in the warm, wet tropics during the Permo-Carboniferous (Macdonald et al. 2019).

During most of the Carboniferous and Permian, CO_2 proxies average about 500 ppm, but with a sharp increase in the Early Triassic (between 240 and 230 Ma) to values of more than 2000 ppm, followed by a decline to values near 1000 ppm by the early Jurassic (Fig. 12e). Through the rest of the Mesozoic and into the Cenozoic the atmospheric CO_2 fluctuated around 1000 ppm (peaking in the Aptian), followed by a decline to near pre-industrial levels in recent times. Cenozoic glaciations are recorded in Antarctica at ~34 Ma (e.g. Kennett 1977; Zachos *et al.* 2001; Katz *et al.* 2008), but it was during the Pliocene at ~2.7 Ma that the first phase of the Plio-Pleistocene glaciations started (Jansen *et al.* 2000; Thiede *et al.* 2011; Bailey *et al.* 2013; De Schepper *et al.* 2014; Bierman *et al.* 2014). A pronounced decline in atmospheric CO_2 played a central role in pre-conditioning the climate for the Plio-Pleistocene glaciation (Fig. 12e).

The Earth's atmosphere circulates as three cells in each hemisphere, i.e. between the intertropical convergence zone (near the Equator) and the subtropical highs at ~30°N/S (Hadley cells), between 30°N/S and ~40°-60°N/S, depending on the season (Ferrell cells), and the Polar

cells above ~40°-60°N/S (see Hay *et al.* 2018). On geological time-scales it has commonly been assumed that climate gradients have remained broadly similar to today, with a stable Hadley circulation, and even on an Earth free of polar ice the subtropical highs should be close to where they are today (~30°N/S). Past climate gradients can be assessed from paleogeographic biome maps. Coals (since the Early Devonian) are commonly confined to near the Equator (humid conditions) or the northerly/southerly wet-belts and indicate a prolonged excess of precipitation over evaporation. Conversely, evaporites are mostly found in the subtropics at mean latitudes of 33° (N/S) for the past 50 Myrs (Fig. 9d) — but mean evaporite latitudes become strikingly lower back in time (Torsvik & Cocks 2017). This is witnessed by absolute mean values of ~24° stretching from the early Paleocene back to Devonian times — except for a pronounced minimum ($17 \pm 9°$) in the Triassic — and then a second shift to even lower mean latitudes before 400 Ma. Thus the tropics appear increasingly more arid back in time (Fig. 9d). This is perhaps unexpected given that the Hadley Cell is currently expanding (e.g. northern hemisphere desert zones spreading and migrating northwards; DeMeo 1989) with global warming, but there are suggestions that Hadley circulation shrank to ~20°N/S latitude during the Middle Cretaceous super-greenhouse (Aptian through Early Coniacian; Hasegawa *et al.* 2012; Hay *et al.* 2018). Lower mean evaporite latitudes of the past may partly reflect the slowing down of Earth: A faster spinning Earth displaces the subtropics equatorward and Christiansen & Stouge (1999) have estimated that the subtropical high was displaced 5° equatorward in Ordovician times (see also Torsvik & Rehnström 2002).

5.3 Paleolatitude of LIP emplacement

Low continental latitudes (and their associated warm and wet climates) promote CO_2 consumption by silicate weathering, and are theoretically associated with low CO_2 periods (Goddéris *et al.* 2014). Enhanced silicate weathering due to LIP emplacement is dependent on many factors, including relief, the area of subaerial exposure, and the latitudinal location of the LIP. Six major Phanerozoic continental LIPs (i.e. Kalkarindji, SCLIP, Emeishan, CAMP, Deccan and Afar) were emplaced within present day tropical latitudes (Fig. 3d), although the wet belts may have been narrower or even absent in the past. With the exception of the Emeishan LIP (Jerram *et al.* 2016a), they were sourced from the margins of TUZO (Fig. 4b). There are of course also continental Precambrian LIPs (Fig. 4a) undergoing weathering today but their areal extent today is less than 10% of the total preserved LIP areas, and exposed basalt substrates become significantly less weatherable with time (Porder *et al.* 2007).

Theoretical silicate weatherability and cooling has been explored by estimating the average continental paleolatitude or average absolute paleolatitude weighted by area (i.e. North and South values collapsed together; Fig. 9a, b), but a better approach is to calculate the fraction of the total continental area that is located in the tropics (currently around ± 23.5°; present axial tilt of the Earth), i.e. subjected to potentially warm and wet climates with high weatherability (Fig. 9c). We notice, however, peaks during both the end-Ordovician glaciation (~50%) and the Triassic-Jurassic greenhouse world (40%). Due to substantial changes in global sea-level (peaking in Ordovician and Cretaceous times, and perhaps 200 meter higher sea-level than present day; Haq & Al-Quhtani 2005; Haq & Shutter 2008) and continental flooding, the *effective* weatherability at tropical latitudes would peak in the Late Triassic, at a time with no evidence for ice. This may suggest, to a first order, that enhanced silicate weathering in the tropics is not fundamentally important in triggering glaciations, but one should keep in mind that the equatorial region of Pangea was dominated by arid conditions in the Late Paleozoic and Early Mesozoic.

Evaporite localities within a single continent can certainly reflect seasonal and local conditions rather than global climatic conditions, but there is ample evidence that Laurentia, Siberia, North and South China and Western Australia defined an extensive, arid, low-latitude evaporite belt in the Early Paleozoic (Fig. 10d). In the Cambrian, Gondwana stretched from the South Pole (Northwest Africa) to the Equator and the ~510 Ma Kalkarindji LIP (Fig. 4a) — sourced from the northeast margin of TUZO (Fig. 4b) — was emplaced over a vast tropical area (>2 million km^2) in Western Australia. However, the widespread evaporite occurrences in Western Australia suggest low weatherability during the late Cambrian and most of the Ordovician. Western Australia, however, appears less arid in Late Ordovician and Early Silurian times (Torsvik & Cocks 2017), which may have resulted in higher weatherability in the low-latitude regions of Gondwana. The end-Ordovician (Hirnantian glaciation) was followed by widespread extinctions near the Ordovician-Silurian boundary (~445 Ma), the first of the "Big Five" Phanerozoic extinctions, which is *not* temporally linked to any known LIP.

The second low-latitude Phanerozoic LIP is the ~300 Ma Skagerrak Centered LIP (SCLIP; Torsvik *et al.* 2008), perhaps affecting an area of ~500,000 km^2 in Scandinavia, Scotland and Northern Germany (Fig. 4a). SCLIP was sourced by a plume from the northeast margin of TUZO (Fig. 4b) and erupted at low latitudes when Central Pangea — including North America and Europe — was located near the Equator (Fig. 10c) and covered by humid tropical rainforest. Latitudinal temperature gradients during the early phase of the Permo-Carboniferous icehouse (~330-275 Ma) were much higher than during the earlier greenhouse periods and

perhaps not dissimilar to the present day (Torsvik & Cocks 2017). As the climate aridified, the rain forests collapsed, and were eventually replaced by seasonally dry biomes in the Early Permian (Sahney *et al.* 2010). The areas that were affected by SCLIP aridified quickly during the Permian, thus weakening the silicate weathering efficiency, and extensive salt basins (Zechstein) covered northwest Europe in Late Permian-Triassic times (Fig. 10a). The Middle-Late Permian was dominated by an expansive arid region that extended across much of Pangea, spanning both northern and southern latitudes, and crossing both the Americas and Europe (Boucot *et al.* 2013; Torsvik & Cocks 2017). Low global climatic gradients and a low latitude arid region traversing most of central Pangea broadly characterized the Triassic and Jurassic, but the arid realm shifted southwards as Pangea moved systematically northwards until the Middle Jurassic (Fig. 9a), when the opening of the Central Atlantic initiated the break-up of the supercontinent. Interestingly, from the Early Devonian (~400 Ma) to the Early Jurassic (~190 Ma), the latitudinal component of the continental center of mass (with respect to the spin axis) has drifted slowly northwards (Fig. 9a) with approximately the same velocity (0.44º/Ma or ~50 km/Ma) ─ and was seemingly unaffected by the formation of Pangea.

The next low-latitude LIP, the Emeishan LIP (ELIP), erupted ~260 Ma (Jerram *et al.* 2016a) and a tropical humid condition at eruption time is evidenced by shallow marine carbonates and widespread coal-measures derived from marine mangrove-like plants (Shao *et al.* 1998). Most of the Emeishan lavas, however, were emplaced at or below sea level, and terrestrial lava flows only developed in the later stages (Ukstins Peate & Bryan 2008; Jerram *et al.* 2016a). South China drifted northwards after the ELIP eruptions; it aridified during the Early Triassic (Fig. 11a), and since the mid-Triassic it has essentially remained in the northern temperate zone. Early Triassic evaporites in South China are clearly anomalous (Boucot *et al.* 2013) as most of the low latitude continental blocks and terranes bordering the Panthalassic Ocean during Late Paleozoic and Early Mesozoic times are characterized by coal deposits, suggesting tropical conditions (e.g., Figs 10c, 11a).

High atmospheric CO_2 levels (~2000 ppm) are indicated from the proxy record from about 230 Ma, declining to ~1000 ppm by about 190 Ma (Early Jurassic) (Fig. 12e). The 201 Ma CAMP was emplaced during this greenhouse period, at low latitudes (Fig. 3d) and it covered a vast area (Fig. 11b), perhaps more than 10 million km^2. Its emplacement in tropical latitudes should theoretically have led to extensive post-emplacement silicate weathering and reduced CO_2 levels (cooling). However, biome maps suggest that the equatorial region of Pangea was dominated by an arid or at least seasonally dry environment at end-Triassic times, with limited evidence for tropical conditions (e.g., coal is found in the southernmost Newark

Basin; Smoot 1991) (Fig. 11b). The end-Triassic and Early Jurassic climate was characterized by low climate gradients with a Pangean low latitude arid region in southernmost North America, North Africa and South America, except a humid realm facing the Panthalassic Ocean along the west coast of central Pangea (Fig. 11b). As with all LIPs it is difficult to determine the timing or the rate of weathering and in contrast to the biome maps, which suggest extensive low-latitude arid regions in Central Pangea, many argue that huge amounts of the CAMP were removed by chemical weathering within a few million years. This is based on observed trends in seawater Sr- and Os-isotope compositions (Cohen & Coe 2007), and carbon-cycle variations in the Newark Basin (Fig. 8c; see below).

The ~66 Ma Deccan Traps, with an estimated subaerial extent of ~1.8 x 10^6 km^2, were emplaced at low southerly latitudes (centred on ~20°S) in tropical humid conditions (widespread coal-measures) and subsequently drifted across the Equator to ~20°N (Fig. 3d) whilst India also collided with Asia in the process to produce the Himalayan orogeny. Finally, Afar was emplaced at low latitudes at 31 Ma (Fig. 3d), and the combined weathering (cooling) effects of the Afar, Deccan and remnants of CAMP (notably in western Africa and northern South America) may have decreased CO_2 levels in the Late Cenozoic (Fig. 10a). However, declining Late Cenozoic CO_2 levels can also be attributed to accelerated continental weathering due to Himalayan mountain building (Raymo *et al.* 1988) and/or increased weathering due to tropical ophiolite obduction over the past 30 Myrs (Macdonald *et al.* 2019).

Elevated silicate weathering associated with the weathering of LIP lavas has been argued for both CAMP and the Deccan Traps. Schaller *et al.* (2011) found that pre-CAMP CO_2 background values of ~2000 ppm approximately doubled in response to magmatic activity but decreased toward pre-CAMP levels in just a few hundred thousand years after each magmatic episode (Fig. 8c), which they interpreted to reflect rapid weathering of fresh CAMP volcanics. Similarly, Dessert *et al.* (2001) modelled an increase in atmospheric CO_2 levels by ~1000 ppm for Deccan, which subsequently was reduced to pre-Deccan levels in about one Myr. Such short-time perturbations are not recognized in the long-term GEOCARBSULF carbon and sulphur cycle model, which estimates atmospheric CO_2 levels in 10 Myr intervals (Royer *et al.* 2014).

CO_2 proxies in Fig. 12e are averaged in 10 Myrs bins and there are two notable CO_2 peaks at 250 Ma (N=5 proxies) and 200 Ma (N=105) that may reflect the influence of the Siberian Traps and the CAMP, respectively. But the most pronounced increase in long-term atmospheric CO_2 is observed between 240 and 230 Ma (Early Triassic). Johansson *et al.* (2017) argued for a strong correlation between the weathering of CAMP and CO_2 proxies from 200

Ma to 100 Ma, but there is no systematic decrease in CO_2 (*"cooling"*) between 190 and 100 Ma (i.e. proxy values, except 160 Ma, statistically overlap at the 95% confidence level; Fig. 12e). We therefore do not see any clear statistical relationship between CAMP ─ presumably one of the largest LIPs in Earth history ─ and very long-term (>10 million years) weathering and potential CO_2 drawdown and cooling.

5.4. GEOCARBSULF: Proxy-model CO₂ mismatches

The proxy-record and atmospheric CO_2 modelled with GEOCARBSULF fits well for the Late Paleozoic (correlation coefficient=0.96; 400-260 Ma) but modelled CO_2 levels from about 200 Ma to 30 Ma (Fig. 12e; black curve with grey confidence envelope) are consistently lower than the proxy record (Royer *et al.* 2014), and thus the correlation coefficient calculated for the past 400 Myrs is low (~0.5). Mismatches can partly be reduced by increased seafloor production rates ─ an important time-dependent plate tectonic degassing parameter (f_{SR}) in the GEOCARBSULF model. Variations in seafloor production (e.g. Coltice *et al.* 2013) can be calculated with sufficient confidence for the last 83 Myrs (after the Cretaceous Normal Superchron) from oceanic lithospheric age-grids estimated from marine magnetic anomalies. Before that time this approach has much larger uncertainties, but because the subduction flux must equal the seafloor production rate (to first order), we can use estimates of the subduction flux derived from full-plate models as a proxy for plate tectonic degassing. van der Meer *et al.* (2014) pursued an even simpler approach: assuming a constant average rate of convergence for subduction zones, globally (specifically 6 cm/yr, the present-day average; Schellart *et al.* 2007), they used normalized subduction lengths through time (estimated back to 235 Ma from seismic tomography) as a proxy for plate tectonic degassing (f_{SR}). This approach was also used by Mills *et al.* (2018), where they used subduction lengths for the past 200 Myr from van der Meer *et al.* (2014), extended backwards with subduction lengths estimated from a plate model (Mills *et al.* 2017), but also combined with normalized rift lengths (Brune *et al.* 2017), assuming that degassing from continental rifts is about one third of that from ridges and arcs. The combined forcing from CO_2 degassing generally yields higher relative degassing than the standard GEOCARBSULF curve (Fig. 12c), but enhanced relative forcing is inadequate to significantly reduce proxy-model discrepancies between 200 and 30 Ma (Mills *et al.* 2018).

The use of subduction lengths as a proxy for the subduction flux requires that the average rate of subduction remains constant through time, but Mesozoic-Cenozoic full-plate models (e.g., Torsvik *et al.* 2010b; Seton *et al.* 2012; Matthews *et al.* 2016) show that high subduction fluxes are often linked to higher average subduction rates rather than to longer

global subduction lengths (Domeier & Torsvik 2017; Hounslow *et al.* 2018). Zircons track past continental arc systems since zircon-fertile rocks are primarily produced along continental subduction zones. From analyses of zircon ages in the context of full-plate tectonic models (back to 410 Ma), we observe that subduction fluxes provide a stronger statistical correlation to zircon age frequency distributions than subduction lengths do, implying that convergence rates play a significant role in regulating the volume of melting in subduction-related magmatic systems (Domeier *et al.* 2018). Zircon age peaks correspond well to intervals of high subduction flux with a ~15 Ma time lag (zircons trailing subduction), and icehouse conditions are associated with lows in zircon age frequency (Fig. 12d). Continental arc-activity has been argued to have played an important role in regulating long-term climate changes (McKenzie *et al.* 2016), i.e. high continental arc activity is linked to warm climate (greenhouses) and reduced arc activity explains icehouse climates. But only the Permo-Carboniferous icehouse shows a clear relation to the zircon record, the end-Cenozoic icehouse occurs long after a major reduction in zircon-age frequencies (starting in the Late Cretaceous), and the end-Ordovician Hirnantian icehouse was followed by ~120 Myrs of low zircon age frequencies when the climate was generally warm, although there are some rocks of glacial origin in the latest Devonian and earliest Carboniferous of South America (Torsvik & Cocks 2017). A minimum in zircon age frequencies is also noticed in Triassic-Jurassic times during greenhouse conditions. The *continental arc magmatic hypothesis* (McKenzie *et al.* 2016), attempting to explain all icehouses by reduced continental arc activity, is partly founded on the idea that arc-related magmatism along continental-margin subduction zones may have contributed 3-5 times more CO_2 to the atmosphere than island arcs because of decarbonation of the continental crust of the overriding plate (e.g. Lee *et al.* 2013; Lee & Lackey 2015; Cao *et al.* 2017).

Modelling atmospheric CO_2 levels for the past 400 Myrs using normalized subduction flux (Table 3) as a time-variable input for f_{SR} in the GEOCARBSULF model reduces model-proxy mismatches in the Middle Triassic and Early Cretaceous (blue curve in Fig. 12e). But large offsets, averaging to 510 ± 458 ppm for the past 400 Myrs, still exist and a distinct peak at 250 Ma (~1900 ppm) is at odds with the proxy record. This modelling peak is coeval with a pronounced zircon age peak, and is close to the smallest of three peaks in the input subduction flux curve (~360, 260 and 130 Ma), but it is apparently controlled by the strength of the silicate weathering feedback. GEOCARBSULF has been revised several times, and an important change in the current version (Royer *et al.* 2014) was the inclusion of new weathering-related inputs based on coupled climate and carbon cycle models (Goddéris *et al.* 2012, 2014). These time-dependent inputs included the land mean surface temperature (GEOG), land area (f_A),

fraction of land area undergoing chemical weathering (f_{Aw}/f_A), and global river runoff (f_D). Interestingly, if we revert to the original GEOCARBSULF inputs for these parameters (Berner 2006), modelled CO_2 (red curve in Fig. 12e) correlates better with proxy data at 250 Ma and the Cretaceous-Early Paleogene, and the magnitude of the modelled carbon CO_2 spikes correlate more linearly to the subduction flux input curve (Fig. 12d,e). Using the original weathering parameters of Berner (2006), however, results in uniformly low modelled CO_2 levels (around 500 ppm) during the Early Mesozoic (240 to 170 Ma) and therefore does not capture the much higher CO_2 greenhouse levels suggested from proxies. Average model-proxy mismatches since the Early Devonian are somewhat reduced (415 ppm) using the old weathering parameters, but the correlation coefficient is lower (0.35) and statistically insignificant.

Runoff is a first-order controlling factor of silicate weathering, and the global runoff model of Berner (1994; 2006) was based on an assumed correlation between temperature and runoff, modulated by a "*continental*" factor that accounted for the effect of paleogeography. In the current GEOCARBSULF version (Royer *et al.* 2014), Phanerozoic silicate weathering parameterizations are derived from 3D climate and carbon-cycle GEOCLIM simulations (Goddéris *et al.* 2014). The only forcing functions in these simulations are the energy input from the Sun (dimmer in the past) and paleogeography taken from many sources (Vrielynck & Bouysse 2003; Blakey 2003, 2008; Sewall *et al.* 2007; Herold *et al.* 2008) but we note that these are much generalized and sometime outdated. As an example, we compare our end-Triassic paleogeography (Torsvik & Cocks 2017) with that used in the Goddéris *et al.* (2014) simulations, and at a time when both weathering models yield much lower modelled CO_2 than proxy values (Fig. 12e). The bulk of Pangea matches our reconstruction but the location of South China is very different; it should be centred on 35°N and not near the Equator as in the GEOCLIM simulation (Fig. 11b). Because it was probably *incorrectly* located in the humid tropical area (as in the Late Paleozoic; Fig. 11a), South China accounted for ~17% of the global CO_2 consumption by silicate weathering at this time. If this added cooling effect is corrected, modelled CO_2 would increase significantly (~500 ppm; Yves Goddéris, pers. comm. 2019) and much better match the Late Triassic-Early Jurassic proxies (Fig. 12e). This single example stresses the importance of accurate paleogeography because it is a prime factor controlling runoff and therefore silicate weathering (Goddéris *et al.* 2014).

6. Concluding remarks and challenges

The connections between the Earth's interior and its surface are manifold, and defined by processes of material transfer: from the deep Earth to lithosphere, through the crust and into the interconnected systems of the atmosphere-hydrosphere-biosphere, and back again. One of the most spectacular surface expressions of such a process, with origins extending into the deep mantle, is the emplacement of LIPs, which have led to rapid climate changes and mass extinctions, but also to moments of transformation with respect to Earth's evolving paleogeography. But equally critical are those process which involve material fluxes going the other way—as best exemplified by subduction, a key driving force behind plate tectonics, but also a key driver for long-term climate evolution through arc volcanism and degassing of CO_2. Below we summarize some of the key aspects among the complex systems and processes that we have addressed.

- Plumes are sourced from specific regions in the deep Earth and mostly from the edges of two quasi-stable thermochemical piles (TUZO and JASON) and they travel from the core-mantle boundary to the base of the lithosphere in about 30 Myrs or less, if the spatial correlation between plume source and the margins of the piles is to be maintained.

- Plumes take us to sub-lithospheric levels where significant partial melting occurs, and to the surface, where hotspot lavas are erupting today, and where episodic kimberlite and especially LIP activity have led to major climate perturbations and Earth crises on very short time-scales. The degree of climate perturbations and mass extinctions probably reflects a combination of LIP-emplacement environment and magma volume, and a key challenge in understanding the short-term LIP-environment connection is the lack of reliable estimates of magma and gas volumes, and their fluxes.

- Hotspot and kimberlite volcanoes generally have relatively small climate effects compared with that of LIPs (because of volumetric and flux differences), but the eruption of large kimberlite clusters, notably in the Cretaceous, could be capable of delivering enough CO_2 to the atmosphere (1000 Gt or more) to trigger sudden global warming events.

- LIPs are episodic but there is a notable concentration in the Cretaceous (145-66 Ma) when also 75% of all known Mesozoic-Cenozoic kimberlites erupted. Considering slab sinking rates, the time basaltic material may remain near the core-mantle boundary and plume ascent rates, we estimate that material transfer through the entire system (i.e. from subduction of crustal materials until their re-eruption at a hotspot via a plume) should take at least 260 Myr. If so, the vast amount of kimberlites and LIPs that surfaced in the

Cretaceous therefore contain material derived from Rheic and Panthalassic oceanic lithosphere, which was subducted before Pangea formed. However, the formation of plumes may also be influenced by mantle flow caused by much younger slabs of perhaps only half that age, which have only sunk to the mid-mantle, without containing any material derived from them.

- LIP activity affects plate tectonics by creating and modifying plate boundaries, best exemplified by the Atlantic bordering continents where LIP activity was followed by continental break-up and seafloor spreading within a few million years. This resulted in LIP fragmentation: for example, CAMP-related magmatism is now scattered across several different plates.

- The long-term climate is largely controlled by plate tectonic forcing, both via sources and sinks ─ e.g. silicate weathering ─ which can be enhanced by extensive blankets of LIP-lava on short (<1 Myr) and potentially much longer time-scales (not well documented). A key challenge in understanding the rate and timing of LIP weathering lies in securing reliable estimates of the original subaerial lava-areas, and improved paleogeographic biome maps to evaluate climate gradients and weatherability in deep time.

- Subduction fluxes derived from full-plate models provide a powerful means of estimating plate tectonic CO_2 degassing (sourcing) through time. These correlate well with zircon age frequency distributions and zircon age peaks clearly correspond to intervals of high subduction flux associated with greenhouse conditions. Lows in zircon age frequency are more variable with links to both icehouse and greenhouse conditions, and only the Permo-Carboniferous icehouse is clearly related to the zircon and subduction flux record. A key challenge is to develop reliable full-plate models before the Devonian in order to consider the subduction flux during the end-Ordovician Hirnantian glaciations, but we also expect refinements in subduction fluxes for Mesozoic-Cenozoic times as more advanced ocean-basin models with intra-oceanic subduction are being developed and implemented in full-plate models.

- The Permo-Carboniferous and end-Cenozoic icehouses correspond to periods of low CO_2 levels and low plate tectonic degassing. Elevated CO_2 values in the Early Triassic may have resulted from a combination of increased plate tectonic degassing (sourcing) and reduced weatherability due to a low latitude arid region running across most of central Pangea.

- Relative degassing estimates based on subduction flux rates are too low to match proxy CO_2 levels for parts of the Mesozoic and notably the Early Cenozoic. Implementing intra-

oceanic subduction histories, adding fluxes from continental rifts and/or explicitly considering the intersection of continental magmatic arcs with carbonate-filled basins through time would almost certainly increase plate tectonic degassing and further minimize existing model-proxy CO_2 mismatches. But there are many other parameters to consider — including the silicate weathering parametrization — which can be improved by better global paleogeographies to estimate theoretical weatherability, and confirmed by biome maps.

Acknowledgement

References

Alvarez, L.W., Alvarez, W., Asaro, F. & Michel, H.V. (1980). Extra-terrestrial cause for the Cretaceous–Tertiary extinction: experimental results and theoretical interpretation. *Science*, 208, 1095–1108.

Austermann, J., Kaye, B.T., Mitrovica, J.X. & Huybers, P. (2014). A statistical analysis of the correlation between Large Igneous Provinces and lower mantle seismic structure. *Geophysical Journal International*, 197, 1–9. doi:10.1093/ gji/ggt500.

Bailey, I., Hole, G.M., Foster, G.L., Wilson, P.A., Storey, C., Trueman, C.N., & Raymo, M.E. (2013). An alternative suggestion for the Pliocene onset of major northern hemisphere glaciation based the geochemical provenance of North Atlantic Ocean ice-rafted debris. *Quaternary Science Reviews*, 75, 181–194.

Bambach, R.K., Knoll, A.H., & Wang, S.C. (2004). Origination, extinction, and mass depletions of marine diversity. *Paleobiology*, 30, 522–542.

Becker, T.W., & Boschi, L. (2002). A comparison of tomographic and geodynamic mantle models. *Geochemistry Geophysics Geosystems*, 3: 1003. doi:10. 1029/2001GC000168.

Beerling, D.J., Harfoot, M., Lomax, B., & Pyle, J.A. (2007). The stability of the stratospheric ozone layer during the end-Permian eruption of the Siberian Traps. *Phil. Transaction Royal Society*, 365, 1843-1866.

Berner, R.A. 1997. The rise of plants and their effect on weathering and atmospheric CO_2. *Science* 276, 544-546.

Berner, R.A. (2004). The Phanerozoic Carbon Cycle: CO_2 and O_2. Oxford University Press, New York.

Berner, R.A. (2006). Inclusion of the weathering of volcanic rocks in the GEOCARBSULF model. *American Journal Science,* 306, 295-302.

Berner, R.A., Lasaga, A.C., & Garrels, R.M. (1983). The carbonate silicate geochemical cycle and its effect on atmospheric carbon dioxide over the past 100 million years. *American Journal Science,* 283, 641-683.

Bierman, P.R., Corbett, L.B., Graly, J.A., Neumann, T.A., Lini, A., Crosby, B.T., & Rood, D.H. (2014). Preservation of a preglacial landscape under the center of the Greenland Ice Sheet. *Science*, 344, 402–405.

Black, B.A., Elkins-Tanton, L.T., Rowe, M.C., & Peate, I.U. (2012). Magnitude and consequences of volatile release from the Siberian traps. *Earth and Planetary Science Letters*, 317, 363–373.

Blakey, R.C. (2003). Carboniferous-Permian Paleogeography of the Assembly of Pangea. In: Wong, T.E. (Ed.), *Fifteenth International Congress on Carboniferous and Permian Stratigraphy* (pp. 443–465). Royal Netherlands Academy of Arts and Sciences, Utrecht, the Netherlands.

Blakey, R.C. (2008). Gondwana paleogeography from assembly to breakup—a 500 m.y. odyssey. *Geological Society America Special Paper,* 441, 1–28.

Boucot, A.J., Xu, C., & Scotese, C.R. (2013). Phanerozoic Paleoclimate: An Atlas of Lithologic Indicators of Climate. *SEPM Concepts in Sedimentology and Paleontology*, 11.

Bryan S.E., Peate I.U., Peate D.W., Jerram D.A., Mawby M.R., Marsh J.S., & Miller J.A. (2010). The largest volcanic eruptions on Earth. *Earth-Science Reviews*, 102 (3-4), 207-229.

Bryan S.E., Riley, T.R., Jerram D.A., Philip T. Leat, P.T., & Stephens, C.J. (2002) Silicic volcanism: an undervalued component of large igneous provinces/volcanic rifted margins. In Menzies, M.A., Klemperer, S.L., Ebinger, C.J. & Baker, J. (Eds.), *Volcanic Rifted Margins* (Vol. 362, pp. 99-120). Geological Society of America Special Paper.

Bluth, G.J.D., & Kump, L.R. (1991). Phanerozoic paleogeology. *American Journal Science*, 291, 284-308

Bond, D.P.G., & Wignall, P.B. (2014). Large igneous provinces and mass extinctions: An update. *Geological Society of America Special Paper*, 505, 29-55.

Bond, D.P.G., & Grasby, S.E. (2017). On the causes of mass extinctions. *Palaeogeography, Palaeoclimatology, Palaeoecology*, 478, 3–29.

Bower, D.J., Gurnis, M., & Seton, M. (2013). Lower mantle structure from paleogeographically constrained dynamic Earth models. *Geochemistry, Geophysics, Geosystems*, 14, 44–63.

Brown R.J., Manya, S., Buisman, I., Fontana, G., Field, M., Mac Niocaill, C., Sparks, R.S.J., & Stuart, F.M. (2012). Eruption of kimberlite magmas: physical volcanology, geomorphology and age of the youngest kimberlitic volcanoes known on earth (the Upper Pleistocene/Holocene Igwisi Hills volcanoes, Tanzania). *Bulletin Volcanology*, 74, 1621-1643. doi:10.1007/s00445-012-0619-8

Brune, S., Williams, S.E., & Müller, R.D. (2017). Potential links between continental rifting, CO2 degassing and climate change through time. *Nature Geoscience*, 10, 941–946.

Bull, A.L., Domeier, M., & Torsvik, T.H. (2014). The effect of plate motion history on the longevity of deep mantle heterogeneities. *Earth and Planetary Science Letters*, 401, 172–182.

Buiter, S.J.H., & Torsvik, T.H. (2014). A review of Wilson Cycle plate margins: a role for mantle plumes in continental breakup along sutures? *Gondwana Research*, 26, 627–653, doi:10.1016/j.gr.2014.02.007.

Burke, K. (2011). Plate Tectonics, the Wilson Cycle, and Mantle Plumes: Geodynamics from the Top. *Annual Review of Earth and Planetary Sciences*, 39, 1–29. doi:10.1146/annurev-earth-040809-152521.

Burke, K., & Torsvik, T.H. (2004). Derivation of large igneous provinces of the past 200 million years from long-term heterogeneities in the deep mantle. *Earth and Planetary Science Letters*, 227, 531–538.

Burke, K., Steinberger, B., Torsvik, T.H., & Smethurst, M.A. (2008). Plume Generation Zones at the margins of Large Low Shear Velocity Provinces on the Core–Mantle Boundary. *Earth Planetary Science Letters*, 265, 49–60. doi:10.1016/j.epsl.2007.09.042.

Campbell, I.H. (2007). Testing the plume theory. *Chemical Geology*, 241, 153-176.

Cao, W., Lee, Cin-Ty A., & Lackey, J.S. (2017). Episodic nature of continental arc activity since 750 Ma: A global compilation. *Earth Planetary Science Letters*, 462, 85-95.

Chandler, M.T., Wessel, P., Taylor, B., Seton, M., Kim, S.-S., & Hyeong, K. (2012). Reconstructing Ontong Java Nui: Implications for Pacific absolute plate motion, hotspot drift and true polar wander. *Earth and Planetary Science Letters*, 331–332, 140–151. doi:10.1016/j.epsl.2012.03.017.

Christiansen, J.L., & Stouge, S. (1999). Oceanic circulation as an element in

palaeogeographical reconstructions: the Arenig (early Ordovician) as an example. *Terra Nova*, 11, 73– 78.

Cízková, H., van den Berg, A.P., Spakman, W. & Matyska, C. (2012). The viscosity of Earth's lower mantle inferred from sinking speed of subducted lithosphere. *Physics of the Earth and Planetary Interiors,* 200–201, 56–62.

Cocks, L.R.M., & Torsvik, T.H. (2002). Earth Geography from 500 to 400 million years ago: a faunal and palaeomagnetic review. *Journal Geological Society London*, 159, 631-644.

Cohen A.S., & Coe A.L. (2007). The impact of the Central Atlantic Magmatic Province on climate and on the Sr- and Os-isotope evolution of seawater. *Palaeogeography Palaeoclimatolology Palaeoecology*, 244, 374-390.

Coltice, N., Bertrand, H., Rey, P., Jourdan, F., Phillips, B.R. & Ricard, Y. (2009). Global warming of the mantle beneath continents back to the Archaean. *Gondwana Research*, 15, 254–266

Coltice, N., Seton, M., Rolf, T., Müller, R.D., & Tackley. P.J. (2013). Convergence of tectonic reconstructions and mantle convection models for significant fluctuations in seafloor spreading. *Earth and Planetary Science Letters*, 383, 92–100

Conrad, C.P., Steinberger, B., & Torsvik, T.H. (2013). Stability of active mantle upwelling revealed by net characteristics of plate tectonics. *Nature*, 498, 479–482. doi:10.1038/nature12203.

Corfu, F., Polteau, S., Planke, S., Faleide, J.I., Svensen, H., Zayoncheck, A., & Stolbov, N. (2013). U-Pb geochronology of Cretaceous magmatism on Svalbard and Franz Josef Land, Barents Sea large igneous province. *Geological Magazine*, 150, 1127–1135. doi:10. 1017/S0016756813000162.

Courtillot, V.E., & Renne, P.R. (2003). On the ages of flood basalt events. *Comptes Rendues Geoscience*, 335, 113-140.

Courtillot, V., Davaille, A., Besse, J., & Stock, J. (2003). Three distinct types of hotspots in the Earth's mantle. *Earth and Planetary Science Letters*, 205, 295–308. doi:10.1016/S0012-821X(02)01048-8.

Davies, D.R., Goes, S., & Sambridge, M. (2015). On the relationship between volcanic hotspot locations, the reconstructed eruption sites of large igneous provinces and deep seismic structure. *Earth Planetary Science Letters*, 411, 121–130. doi:10.1016/j.epsl.2014.11.052.

Dawson J.B. (1994). Quaternary kimberlitic volcanism on the Tanzania craton. *Contributions Mineral Petrology*, 116, 473-485.

DeMeo J. (1989). Desert expansion and drought: environmental crisis, Part I. *Journal Orgonom*, 23, 15–26.

De Schepper, S., Gibbard, P.L., Salzmann, U., & Ehlers, J. (2014). A global synthesis of the marine and terrestrial evidence for glaciation during the Pliocene Epoch. *Earth-Science Reviews*, 135, 83–102.

Dessert, C., Dupré, B., François, L.M., Schott, J., Gaillardet, J., Chakrapani, G., & Bajpai, S. (2001). Erosion of Deccan Traps determined by river geochemistry: impact on the global climate and the $^{87}Sr/^{86}Sr$ ratio of seawater. *Earth and Planetary Science Letters*, 188(3-4), 459-474.

Dessert, C., Dupré, B., Gaillardet, J., François, L.M., & Allègre, C.J. (2003). Basalt weathering laws and the impact of basalt weathering on the global carbon cycle. *Chemical Geology*, 202, 257-273.

Dickens G.R., J.R. O'Neil, D.K. Rea & R.M. Owen (1995). Dissociation of oceanic methane hydrate as a cause of the carbon isotope excursion at the end of the Paleocene. *Paleoceanography*, 10, 965–971.

Domeier, M. (2015). A plate tectonic scenario for the Iapetus and Rheic oceans. *Gondwana Research*, 36, 275-295. doi:10.1016/j. gr.2015.08.003.

Domeier, M. & Torsvik, T.H. (2014). Plate tectonics in the late Paleozoic. *Geoscience Frontiers*, 5, 303–350.

Domeier, M., & Torsvik, T.H. (2017). Full-plate modelling in pre-Jurassic time. *Geological Magazine Special Issue.* doi:10.1017/S0016756817001005.

Domeier, M., Doubrovine, P.V., Torsvik, T.H. Spakman, W., & Bull, A.L. (2016). Global correlation of lower mantle structure and past subduction. *Geophysical Research Letters*, 43, 4945-4953. doi:10.1002/2016GL068827.

Domeier, M., Magni, V., Hounslow, M.W., & Torsvik, T.H. (2018). Episodic zircon age spectra reflect true fluctuations in global subduction. *Science Reports, 8. 17471,* doi:10.1038/s41598-018-35040-z.

Doubrovine, P.V., Steinberger, B., & Torsvik, T.H. (2012). Absolute plate motions in a reference frame defined by moving hotspots in the Pacific, Atlantic and Indian oceans. *Journal of Geophysical Research*, 117, B09101. doi:10.1029/ 2011JB009072.

Doubrovine, P.V., Steinberger, B., & Torsvik, T.H. (2016). A failure to reject: Testing the correlation between large igneous provinces and deep mantle structures with EDF statistics. *Geochemistry Geophysics Geosystems*, 17, 1130–1163. doi:10.1002/2015GC006044.

Dziewonski, A.M., & Anderson, D.L. (1981). Preliminary Reference Earth Model. *Physics of the Earth and Planetary Interior*, 25, 297–356.

Ernst R.E. (2014). *Large Igneous Provinces*. Cambridge University Press, London.

Ernst, R.E., & Buchan, K.L. (2001). Large mafic magmatic events through time and links to mantle plume-heads. In R.E. Ernst and K.L. Buchan (Eds.), *Mantle Plumes: Their Identification Through Time* (Vol. 352, Chapter 19). Geological Society of America Special Paper.

Faleide, J.I., Bjørlykke, K., & Gabrielsen, R.H. (2010). Geology of the Norwegian Continental Shelf. In K. Bjørlykke (Ed.), *Petroleum Geoscience: From Sedimentary Environments to Rock Physics* (pp.467-499). Springer Science Business Media.

Flament, N., Williams, S., Müller, R.D., Gurnis, M., & Bower, D.J. (2017). Origin and evolution of the deep thermochemical structure beneath Eurasia. *Nature Communications*, 8, 14164. doi:10.1038/ncomms14164.

Foster, G.L., Royer, D.L., & Lunt, D.J. (2017). Future climate forcing potentially without precedent in the last 420 million years: *Nature Communications*, 8, 14845, doi:14810.11038/ncomms14845.

French, S.W., & Romanowicz, B. (2015). Broad plumes rooted at the base of the Earth's mantle beneath major hotspots. *Nature*, 525, 95–99.

Gaillardet, J., Dupré, B., Louvat, P., & Allègre, C.J. (1999). Global silicate weathering and CO_2 consumption rates deduced from the chemistry of large rivers. *Chemical Geology*, 159, 3-30.

Gaina, C., Torsvik, T.H., van Hinsbergen, D.J.J., Medvedev, S., Werner, S.C., & Labails, C. (2013). The African Plate: a history of oceanic crust accretion and subduction since the Jurassic. *Tectonophysics, 604, 4-25*.

Ganino, C., & Arndt, N.T. (2009). Climate changes caused by degassing of sediments during the emplacement of large igneous provinces. *Geology*, 37, 323–326

Garnero, E.J., Lay, T., & McNamara, A. (2007). Implications of lower mantle structural heterogeneity for existence and nature of whole mantle plumes. *Geological Society of America Special Paper*, 430, 79–102. doi:10.1130/2007. 2430(05).

Garnero, E.J., McNamara, A.K. & Shim, S.H. (2016). Continent-sized anomalous zones with low seismic velocity at the base of Earth's mantle. *Nature Geoscience*, 9, 481-489.

Gibbs, M.T., Bluth, G.J.S., Fawcett, P.J., & Kump, L.R. (1999). Global chemical erosion over the last 250 My: variations due to changes in paleogeography, paleoclimate, and paleogeology. *American Journal Science,* 299, 611–651.

Gibbs, M.T., Bice, K.L., Barron, E.J., & Kump, L.R. (2000). Glaciation in the early Paleozoic 'greenhouse': the roles of paleogeography and atmospheric CO_2. In Huber, B.T., MacLeod, K. G., & Wing, S.L. (Eds.), *Warm Climates in Earth History* (p. 386-422). Cambridge, Cambridge University Press.

Goddéris, Y., Donnadieu, Y., Lefebvre, V., Le Hir, G., & Nardin, E. (2012). Tectonic control of continental weathering, atmospheric CO_2, and climate over Phanerozoic times: *Comptes Rendus Geoscience*, 344, 652–662.

Goddéris, Y., Donnadieu, Y., Le Hir, G., Lefebvre, V., & Nardin, E. (2014). The role of palaeogeography in the Phanerozoic history of atmospheric CO_2 and climate. *Earth-Science Reviews,* 128, 122–138.

Goes, S., Agrusta, R., van Hunen, J. & Garel, F. 2017. Subduction-transition zone interaction: A review. *Geosphere* 13(3), 644–664.

Gubanov, A.P., & Mooney, W.D. (2009). New global maps of crustal basement age. Eos Transactions. American Geophysical Union, 90 (Fall Meeting Supplement, Abstract T53B-1583).

Hager, B. H., & O'Connell, R.J. (1979). Kinematic models of large-scale mantle flow. *Journal of Geophysical Research*, 84, 1031–1048.

Hager, B. H., & O'Connell, R.J. (1981). A simple global model of plate dynamics and mantle convection. *Journal of Geophysical Research*, 86, 4843–4867.

Hasegawa, H., Tada, R., Jiang, X., Suganuma, Y., Imsamut, S., Charusiri, P., Ichinnorov, N., & Khand Y. (2012). Drastic shrinking of the Hadley circulation during the mid-Cretaceous Supergreenhouse. *Climate Past*, 8, 1323–1337.

Haq, B.U. & Al-Qahtani, A.M. (2005). Phanerozoic cycles of sea-level change on the Arabian Platform. *GeoArabia*, 10, 127-160.

Haq, B.U. & Shutter, S.R. (2008). A chronology of Paleozoic sea-level changes. *Science*, 322, 64-68.

Hassan, R., Müller, R.D., Gurnis, M., Williams, S.E., & Flament, N.A (2016). Rapid burst in hotspot motion through the interaction of tectonics and deep mantle flow. *Nature*, 533, 239–241.

Hawley, S.M., Pogge von Strandmann, P.A.E., Burton, K.W., Williams, H.M., & Gislason, S.R. (2017). Continental weathering and terrestrial (oxyhydr)oxide export: Comparing glacial and non-glacial catchments in Iceland. *Chemical Geology*, 462, 55-66.

Hay, W.W., DeConto, R.M., de Boer, P.L., Flögel, S., Song, Y., & Stepashk, A. (2018). Possible solutions to several enigmas of Cretaceous climate. *International Journal of Earth Sciences*. doi.org/10.1007/s00531-018-1670-2

Heimdal, T.H., Callegaro, S., Svensen, H.H., Jones, M.T., Pereira, E., & Planke, S. (2019). Evidence for magma–evaporite interactions during the emplacement of the Central Atlantic Magmatic Province (CAMP) in Brazil. *Earth and Planetary Science Letters*, 506, 476–492.

Herold, N., Seton, M., Müller, R.D., You, Y., & Huber, M. (2008). Middle Miocene tectonic boundary conditions for use in climate models. *Geochemistry Geophysics Geosystems*, 9, Q10009.

Herrmann, A. D., Patzkowsky, M. E., & Pollard, D. 2003, Obliquity forcing with 8-12 times preindustrial levels of atmospheric pCO$_2$ during the Late Ordovician glaciation. *Geology* 31, 485-488.

Hounslow, M., Domeier, M., & Biggin, A.J. (2018). Subduction flux modulates the geomagnetic polarity reversal rate. *Tectonophysics,* 742-743, 34-49.

Hosseini, K., Matthews, K.J., Sigloch, K., Shephard, G.E., Domeier, M. & Tsekhmistrenko, M. (2018). SubMachine: Web-Based tools for exploring seismic tomography and other models of Earth's deep interior. *Geochemistry, Geophysics, Geosystems*, 19, 1464-1483.

Jansen, E., Fronval, T., Rack, F., & Channell, J.E.T. (2000). Pliocene-Pleistocene ice rafting history and cyclicity in the Nordic Seas during the last 3.5 Myr. *Paleoceanography*, 15, 709–721.

Japsen, P., Chalmers, J.A., Green, P.F., & Bonow, J.M. (2011). Elevated, passive continental margins: Not rift shoulders, but expressions of episodic, post-rift burial and exhumation. *Global and Planetary Change*, 90-91, 73-86. doi:10.1016/j.gloplacha.2011.05.004.

Jerram D.A., Dobson, K.J., Morgan, D.J., & Pankhurst, M.J. 2018. The Petrogenesis of Magmatic Systems: Using Igneous Textures to Understand Magmatic Processes. In S. Burchardt (Ed.), *Volcanic and Igneous Plumbing Systems* (pp. 191-229). Elsevier. ISBN 9780128097496,https://doi.org/10.1016/B978-0-12-809749-6.00008-X.

Jerram D.A., Widdowson, M., Wignall, P.B., Sun, Y., Lai, X., Bond, D.P.G., & Torsvik, T.H. (2016a). Submarine palaeoenvironments during Emeishan flood basalt volcanism, SW China: Implications for plume–lithosphere interaction during the Capitanian, Middle Permian ('end Guadalupian') extinction event. *Palaeogeography, Palaeoclimatology, Palaeoecology*, 441 (1), 65-73.

Jerram D.A., Svensen, H.H., Planke, S., Polozov, A.G., & Torsvik, T.H. (2016b). The onset of flood volcanism in the north-western part of the Siberian Traps: Explosive volcanism versus effusive lava flows. *Palaeogeography, Palaeoclimatology, Palaeoecology*, 441 (1), 38–50.

Jerram D.A., Mock, A., Davis, GR., Field, M., & Brown, R.J. (2009). 3D crystal size distributions: A case study on quantifying olivine populations in kimberlites. *Lithos*, 112, 223–235.

Jerram D.A., & Widdowson, M. (2005). The anatomy of Continental Flood Basalt Provinces: Geological constraints on the processes and products of flood volcanism. *Lithos*, 79, 385-405.

Jerram D.A., Davis, G.R., Mock, A., Charrier, A., & Marsh, B.D. (2010). Quantifying 3D crystal populations, packing and layering in shallow intrusions: a case study from the Basement Sill, Dry Valleys, Antarctica. *Geosphere*, 6 (5), 537-548.

Johansson, L., Zahirovic, S., & Müller, R.D. (2017). The interpay between the eruption of large igneous prvinces and the deep-time carbon cycle. *Geophysical Research Lettetters*, 45, 5380-5389.

Jones, M.T., Jerram, D.A., Svensen, H.H., & Grove, C. (2016). The effects of large igneous provinces on the global carbon and sulphur cycles. *Palaeogeography Palaeoclimatolology Palaeoecolology*, 441, 4–21.

Jones, M.T., Percival, L.M.E., Stokke, E.W., Frieling, J., Mather, T.A., Riber, L., Schubert, B.A., Schultz, B., Tegner, C., Planke, S., & Svensen, H.H. (2019). Mercury anomalies across the Palaeocene-Eocene Thermal Maximum. *Climate of the Past*, 15, 217-236.

Jourdan, F., Féraud, G., Bertrand, H., Kampunzu, A.B., Tshoso, G., Watkeys, M.K., & Le Gall, B. (2005). Karoo large igneous province: brevity, origin, and relation to mass extinction questioned by new ^{40}Ar/^{39}Ar age data. *Geology*, 33, 745–748.

Julian, B., Foulger, G., Hatfield, O., Jackson, S., Simpson, E., Einbeck, J., & Moore, A. (2015). Hotspots in Hindsight. *Geological Society of America Special Paper*, 514, 105–121. doi:10.1130/2015.2514(08).

Katz, M.E., Miller, K.G., Wright, J.D., Wade, B.S., Browning, J.V., Cramer, B.S., & Rosenthal, Y. (2008). Stepwise transition from the Eocene greenhouse to the Oligocene icehouse. *Nature Geoscience*, 1,329-334.

Kennett, J.P. (1977). Cenozoic evolution of Antarctic glaciations, the circum-Antarctic ocean and their impact on global paleoceanography. *Journal of Geophysical Research*, 82, 3843–3860.

Kent D.V. (2003). A case for a comet impact trigger for the Paleocene/Eocene thermal maximum and carbon isotope excursion. *Earth and Planetary Science Letters*, 211, 13–26.

Kurtz A.C., L.R. Kump, M.A. Arthur, J.C. Zachos & A. Paytan (2003). Early Cenozoic decoupling of the global carbon and sulfur cycles. *Paleoceanography*, 18(4), 1090.

Labails, C., Olivet, J.L., Aslanian, D., & Roest, W.R. (2010). An alternative early opening scenario for the Central Atlantic Ocean. *Earth and Planetary Science Letters*, 297, 355–368.

Lee, C.-T. A., & Lackey, J.S. (2015). Global Continental Arc Flare-ups and Their Relation to Long-Term Greenhouse Conditions. *Elements*, 11, 125–130.

Lee, C.-T. A., Shen, B., Slotnick, B.S., Liao, K., Dickens, G.R., Yokoyama, Y., Lenardic, A., dasgupta, R., Jellinek, M., Lackey, J.S., Schneider, T., & Tice, M.M. (2013). Continental arc–island arc fluctuations, growth of crustal carbonates, and long-term climate change. *Geosphere,* 9, 21–36.

Lin, S.C., & van Keken, P.E. (2006). Dynamics of thermochemical plumes: 2. Complexity of plume structures and its implications for mapping mantle plumes, *Geochemistry Geophysics Geosystems*, 7, Q03003, doi:10.1029/2005GC001072.

Liu, L., Gurnis, M., Seton, M., Saleeby, J., Muller, R.D., & Jackson J.M. (2010). The role of oceanic plateau subduction in the Laramide orogeny. *Nature Geoscience*, 3, 353–357, doi:10.1038/NGEO829.

Liu, W., Shi, C., Xu, Z., Zhao, T., Jiang, H., Liang, C., Zhang, X., Zhou, L., & Yu, C. (2016). Water geochemistry of the Qiantangjiang River, East China: Chemical weathering and CO_2 consumption in a basin affected by severe acid deposition. *Journal of Asian Earth Sciences*, 127, 246-256.

Lowry, D.P, Poulsen, C.J., Horton, D.E., Torsvik, T.H., & Pollard, D. (2014). Thresholds for Paleozoic ice sheet initiation. *Geology*, 42; 627–630.

Macdonald, F.A., Swanson-Hysell, N.L., Park, Y., Lisiecki, L. & Jagoutz, O. (2019). Arc-continent collisions in the tropics set Earth's climate state. *Science* 364, 181-184.

Madrigal, P., Gazel, E., Flores, K., Bizimis, M. & Jicha, B. (2016). Record of massive upwellings from the Pacific large low shear velocity province. *Nature Communications* 7: 13309.

Marshall, H.G., Walker, J.C.G., & Kuhn, W.R. (1988). Long-term climate change and the geochemical cycle of carbon. *Journal of Geophysical Research*, 93, 791–801.

Marzoli A. Callegaro, S., Dal Corso, J., Davies, J.H.F.L., Chiaradia, M., Youbi, N., Bertrand, H., Reisberg, L., Merle, R., & Jourdan, F. (2018). The Central Atlantic Magmatic Province

(CAMP): A Review. In: Tanner L. (Ed.), *The Late Triassic World. Topics in Geobiology* (Vol. 46). Springer, Cham

Matthews, K., Maloney, K.T., Zahirovic, S.,Williams, S.E., Seton, M., & Müller, R.D. (2016). Global plate boundary evolution and kinematics since the late Paleozoic. *Global and Planetary Change,* 146, 226–250.

McGhee, G.R., Clapham, M.E., Sheehan, P.M., Bottjer, D.J., & Droser, M.L. (2013). A new ecological-severity ranking of major Phanerozoic biodiversity crises. *Palaeogeography Palaeoclimatology Palaeoecology*, 370, 260–270.

McKenzie, N.R., Horton, B.K., Loomis, S.E., Stockli, D.F., Planavsky, N.J., & Lee, C-T. (2016). Continental arc volcanism as the principal driver of icehouse-greenhouse variability. *Science*, 352, 444-447.

Mills, B.J.W., Scotese, C.R., Walding, N.G., Shields, G.A., & Lenton, T.M. (2017). Elevated CO_2 degassing rates prevented the return of Snowball Earth during the Phanerozoic. *Nature Communications.* dOI:10.1038/s41467-017-01456-w

Mills, B.J.W., Krause, A.J., Scotese, C.R., Hill, D.J., Shields, G.A., & Lenton, T.M. (2019). Modelling the long-term carbon cycle, atmospheric CO_2, and Earthsurface temperature from late Neoproterozoic to present day. *Gondwana Research*, 67, 172–186

Mitchell, R.H. (1986). Kimberlites: Mineralogy. Geochemistry and Petrology (Plenum).

Milliman, J., & Farnsworth, K.L. (2011). River Discharge to the Coastal Ocean: A Global Synthesis. Cambridge University Press.

Morgan, W.J. (1971). Convection plumes in the lower mantle. *Nature*, 230, 42–43. doi:10.1038/230042a0.

Morgan, W.J., & Morgan, J.P. (2007). Plate velocities in the hotspot reference frame. In Foulger, G.R., & Jurdy, D.M. (Eds.), *Plates, Plumes, and Planetary Processes* (Vol. 430, pp. 65–78). Geological Society of America Special Paper. doi:10.1130/2007.2430(04).

Mulyukova, E., Steinberger, B., Dabrowski, M., & Sobolev, S.V. (2015a). Survival of LLSVPs for billions of years in a vigorously convecting mantle: replenishment and destruction of chemical anomaly. Journal of Geophysical Research: *Solid Earth*, 120, 3824–3847. doi:10.1002/2014JB011688.

Mulyukova, E., Steinberger, B., Dabrowski, M., & Sobolev, S.V. (2015b). Residence time of oceanic crust in the deep mantle. GRC - Gordon Research Conferences, South Hadley, MA, USA.

Nardin, E., Goddéris, Y., Donnadieu, Y., Le Hir, G., & Blakey, R.C. (2011). Modeling the early Paleozoic long-term climatic trend. *Geological Society of America Bulletin.* doi: 10.1130/B30364.1

Osmundsen, P.T. & Redfield, T.F. (2011). Crustal taper and topography at passive continental margins. *Terra Nova,* 23 (6).

Otto-Bliesner, B.L. (1995). Continental drift, runoff, and weathering feedbacks: Implications from climate model experiments. *Journal of Geophysical Research*, 100, 11,537-11,548

Panasyuk, S.V., Hager, B.H., & Forte, A.M. (1996), Understanding the effects of mantle compressibility on geoid kernels. *Geophysical Journal International*, 124, 121-133. doi:10.1111/j.1365-246X.1996.tb06357.x

Patterson M.V. & Francis, D. (2013). Kimberlite eruptions as triggers for early Cenozoic hyperthermals. *Geochemistry Geophysics Geosystems*, 14, 448–456, doi:10.1002/ggge.20054.

Percival, L.M.E., Witt, M.L.I., Mather, T.A., Hermoso, M., Jenkyns, H.C., Hesselbo, S.P., Al-Suwaidi, A.H., Storm, M.S., Xu, W. & Ruhl, M. (2015). Globally enhanced mercury deposition during the end-Pliensbachian extinction and Toarcian OAE: a link to the Karoo-Ferrar Large Igneous Province. *Earth and Planetary Science Letters*, 428, 267–280.

Porder, S., Hilley, G.E., & Chadwick, O.A. (2007). Chemical weathering, mass loss, and dust inputs across a climate by time matrix in the Hawaiian Islands. *Earth and Planetary Science Letters*, 258, 414–427.

Rampino, M.R., Self, S., & Stothers, R.B. (1988). Volcanic winters. *Annual Review of Earth and Planetary Sciences*, 16, 73-99.

Raymo, M.E., Ruddiman, W.F., & Froelich, P.N. 1988. Influence of late Cenozoic mountain building on ocean geochemical cycles. *Geology*, 16, 649–653.

Redfield, T.F. & Osmundsen, P.T. (2012). The long-term topographic response of a continent adjacent to a hyperextended margin: A case study from Scandinavia. *Geological Society of America Bulletin,* 125 (1-2).

Richards, M.A., & Griffiths, R.W. (1988). Deflection of plumes by mantle shear flow: experimental results and a simple theory. *Geophysical Journal International*, 94, 367–376.

Richards, M.A., Hager, B.H., & Sleep, N.H. (1988). Dynamically supported geoid highs over hotspots: Observations and theory: *Journal of Geophysical Research*, 93, 7690–7708. doi:10.1029/JB093iB07p07690.

Richards, M.A., Duncan R.A., & Courtillot V.E. (1989). Flood basalts and hot-spot tracks: plume heads and tails. *Science*, 246, 103-107.

Robock, A. (2000). Volcanic eruptions and climate. *Reviews of Geophysics*, 38 (2), 191–219.

Ronov, A.B. (1994). Phanerozoic transgressions and regressions on the continents; a quantitative approach based on areas flooded by the sea and areas of marine and continental deposition. *American Journal Science*, 294, 777–801. doi:10.2475/ajs.294.7.777

Royer D.L. (2006). CO_2-forced climate thresholds during the Phanerozoic. *Geochimica et Cosmochimica Acta*, 70, 5665-5675.

Royer, D.L., Donnadieu Y., Park, J., Kowalczyk, J., & Goddéris Y. (2014). Atmospheric CO_2 and O_2 during the Phanerozoic: Tools, Patterns, and Impacts. *Treatise on Geochemistry* 251-266.

Russell, J.K. Porritt, L.A., Lavallée, Y., Dingwell, D.B. (2012). Kimberlite ascent by assimilation-fuelled buoyancy. *Nature*, 481, 352-356.

Sahney, S., Benton, M.J., & Falcon-Lang, H.J. (2010). Rainforest collapse triggered Carboniferous tetrapod diversification in Euramerica. *Geology*, 38, 1079–1082.

Sanei, H., Grasby, S., & Beauchamp, B. (2012). Latest Permian mercury anomalies. *Geology*, 40, 63-66.

Seton, M., Müller, R.D., Zahirovic, S., Gaina, C., Torsvik, T.H., Shephard, G., Talsma, A., Gurnis, M., Turner, M., Maus, S., & Chandler, M. (2012). Global continental and ocean basin reconstructions since 200 Ma. *Earth-Science Reviews,* 113, 212–270.

Sewall, J.O., van deWal, R.S.W., Zwan, K.V.D., Oosterhout, C.V., Dijkstra, H.A., & Scotese, C.R. (2007). Climate model boundary conditions for four Cretaceous time slices. *Climate Past*, 3, 647–657.

Schaller, M.F., Wright, J.D., & Kent, D.V. (2011). Atmospheric *P*CO2 Perturbations Associated with the Central Atlantic Magmatic Province. *Science*, 331, 1404-1409.

Schellart, W., Stegman, D., & Freeman, J. (2008). Global trench migration velocities and slab migration induced upper mantle volume fluxes: constraints to find an Earth reference frame based on minimizing viscous dissipation. *Earth-Science Reviews,* 88, 118–44.

Schmidt, A., Carslaw, K.S., Mann, G.W., Rap, A., Pringle, K.J., Spracklen, D.V., Wilson, M., & Forster, P.M. (2012). Importance of tropospheric volcanic aerosol for indirect radiative forcing of climate. *Atmospheric Chemistry and Physics*, 12, 7321-7339.

Scotese, C.R., & Golonka, J. (1992). Paleogeographic Atlas, *PALEOMAP Progress Report 20–0692*, Department of Geology, University of Texas at Arlington, Texas (34 pp.).

Self, S., Keszthelyi, L., & Thordarson, T. (1998). The importance of pahoehoe. *Annual Reviews Earth Planetary Sciences*, 26, 81-110.

Sepkoski Jr., J.J. (1996). Patterns of Phanerozoic extinction: a perspective from global data bases. In: Walliser, O.H. (Ed.), Global Events and Event Stratigraphy in the Phanerozoic. Springer-Verlag, Berlin, pp. 35–51.

Shao, L., Zhang, P., Ren, D., & Lei, J. (1998). Late Permian coal-bearing carbonate successions in southern China: coal accumulation on carbonate platforms. *International Journal Coal Geology*, 37, 235–256.

Shellnutt, J.G., Bhat, G.M, Brookfield, M.E., & Jahn, B-M. (2011). No link between the Panjal Traps (Kashmir) and the Late Permian mass extinctions. *Geophysical Research Letters*, 38, L19308, doi:10.1029/2011GL049032.

Sigloch, K., & Mihalynuk, M.G. (2013). Intra-oceanic subduction shaped the assembly of Cordilleran North America. *Nature*, 496, 50–56. doi:10.1038/nature12019.

Sleep, N.H. (1990). Hotspots and mantle plumes: Some phenomenology: *Journal of Geophysical Research*, 95, 6715–6736. doi:10.1029/JB095iB05p06715.

Sleep, N.H. (1997). Lateral flow and ponding of starting plume material. *Journal of Geophysical Research*, 102, 10001–10012.

Smoot, J.P. (1991). Sedimentary facies and depositional environments of early Mesozoic Newark Supergroup basins, eastern North America. *Paleogeography, Paleoclimatology, and Paleoecology*, 84, 369-423.

Sobolev, S.V., Sobolev, A.V., Kuzmin, D.V., Krivolutskaya, N.A., Petrunin, A.G., Arndt, N.T., Radko, V.A., & Vasiliev, Y.R. (2011). Linking mantle plumes, large igneous provinces and environmental catastrophes. *Nature*, 477, 312-316.

Spence, J., & Telmer, K. (2005). The role of sulphur in chemical weathering and atmospheric CO_2 fluxes: Evidence from major ions, $\delta^{13}C_{DIC}$, and $\delta^{34}S_{SO4}$ in rivers of the Canadian Cordillera. *Geochimica et Cosmochimica Acta*, 69 (23), 5441-5458

Stanley, S.M. (2016). Estimates of the magnitudes of major marine mass extinctions in earth history. *Proceedings National Academy of Sciences* USA., 113, E6325–E6334.

Steinberger, B. (2000). Plumes in a convecting mantle: Models and observations for individual hotspots. *Journal of Geophysical Research: Solid Earth*, 105, 11127–11152. doi:10.1029/1999JB900398.

Steinberger, B. (2007). Effect of latent heat release at phase boundaries on flow in the Earth's mantle, phase boundary topography and dynamic topography at the Earth's surface. *Physics of the Earth and Planetary Interior*, 164, 2–20.

Steinberger, B., & O'Connell, R.J. (1998). Advection of plumes in mantle flow: implications on hotspot motion, mantle viscosity and plume distribution. *Geophysical Journal International*, 132, 412–434. doi:10.1046/j.1365-246x.1998. 00447.x.

Steinberger, B., & Antretter, M. (2006). Conduit diameter and buoyant rising speed of mantle plumes: Implications for the motion of hotspots and shape of plume conduits. *Geochemistry Geophysics Geosystems*, 7(1), Q11018, doi:10.1029/2006GC001409

Steinberger, B., & Calderwood, A. (2006). Models of large-scale viscous flow in the Earth's mantle with constraints from mineral physics and surface observations. *Geophysical Journal International*, 167, 1461–1481.

Steinberger, B., & Holme, R. (2008). Mantle flow models with core-mantle boundary constraints and chemical heterogeneities in the lowermost mantle. *Journal of Geophysical Research*, 113, B05403, doi:10.1029/2007JB005080.

Steinberger, B., & Torsvik, T.H. (2012). A geodynamic models of plumes from the margins of Large Low Shear Velocity Provinces. *Geochemistry Geophysics Geosystems*, 13, Q01W09. doi:10.1029/2011GC003808.

Steinberger, B., Sutherland, R., & O'Connell, R.J. (2004). Prediction of Emperor-Hawaii seamount locations from a revised model of global plate motion and mantle flow. *Nature*, 430, 167–173. doi:10.1038/nature02660. PMID:15241405.

Steinberger, B., Torsvik, T.H. & Becker, T.W., 2012. Subduction to the lower mantle - a comparison between geodynamic and tomographic models, Solid Earth, 3, 415-432.

Steinberger, B., Spakman, W., Japsen, P., & Torsvik, T.H. (2015). The key role of global solid-Earth processes in preconditioning Greenland's glaciation since the Pliocene. *Terra Nova*, 27, 1–8.

Svensen, H. Planke, S. & Malthe-Sørensen, A. (2004). Release of methane from a volcanic basin as a mechanism for initial Eocene global warming. *Nature*, 429 (6991), 542–545.

Svensen, H., & Jamtveit, B. (2010). Metamorphic fluids and global environmental changes. *Elements*, 6*, 179-182.*

Svensen, H., Planke, S., & Corfu, F. (2010). Zircon dating ties NE Atlantic sill emplacement to initial Eocene global warming. *Journal of the Geological Society London*, 167, 433–436.

Svensen, H., Corfu, F., Polteau, S., Hammer, Ø. & Planke, S. (2012). Rapid magma emplacement in the Karoo Large Igneous Province. *Earth and Planetary Science Letters*, 325-326, 1-9.

Svensen, H., Jamtveit, B., Planke, S., & Chevallier, L. (2006). Structure and evolution of hydrothermal vent complexes in the Karoo Basin, South Africa. *Journal Geological Society London*, 163, 671-682.

Svensen, H.H**.**, Jerram, D.A., Polozov, A.G., Planke, S., Neal, C.R., Augland, L.E., & Emeleus, H.C. (2019) Thinking about LIPs: A brief history of ideas in Large igneous province research. *Tectonophysics*. doi:10.1016/j.tecto.2018.12.008.

Svensen, H. et al. (2009). Siberian gas venting and the end-Permian environmental crisis. *Earth Planetary Science Letter*s, 277 (3), 490–500.

Svensen, H., Aarnes, I., Podladchikov, Y.Y., Jettestuen, E., Harstad, C.H., & Planke, S. (2010). Sandstone dikes in dolerite sills: evidence for high-pressure gradients and sediment mobilization during solidification of magmatic sheet intrusions in sedimentary basins. *Geosphere*, 6 (3), 211–224.

Svensen, H.H., Torsvik, T.H., Callegaro, S., Augland, L., Heimdal, T.H., Jerram, D.A., Planke, S., & Pereira, E. (2018). Gondwana LIPs: plate reconstructions, volcanic basins and sill volumes. In Sensarma, S., Storey, B.C. (Eds.), *Large Igneous Provinces from Gondwana and Adjacent Regions* (Vol. 463, pp.17–40). The Geological Society of London Special Publications.

Tappe, S., Smart, K.A., Torsvik, T.H., Massuyeau, M., & de Wit, M. (2018). Geodynamics of kimberlites on a cooling Earth: Clues to plate tectonic evolution and deep volatile cycles. *Earth Planetary Science Letters*, 484, 1–14.Tarduno, J.A., Brinkman, D.B., Renne, P.R. et al. (1998). Late Cretaceous Arctic volcanism: tectonic and climatic connections. In American Geophysical Union Spring Meeting Abstracts, Washington, DC: American Geophysical Union.

Taylor, B. (2006). The single largest oceanic plateau: Ontong Java–Manihiki–Hikurangi. *Earth and Planetary Science Letters*, 241, 372–380.

Tegner, C., Andersen, T.B., Kjøll, H.J., Brown, E.L., Hagen - Peter, G., Corfu, F., Planke, S. & Torsvik, T.H. (2019). A mantle plume origin for the Scandinavian Dyke Complex: A "piercing point" for 615 Ma plate reconstruction of Baltica? *Geochemistry, Geophysics, Geosystems* 20. doi:10.1029/2018GC007941.

Thiede, J., Jessen, C., Knutz, P. & et al. (2011). Millions of Years of Greenland Ice Sheet History Recorded in Ocean Sediments. *Polarforschung*, 80, 141–159.

Thompson, D.W.J, Wallace, J.M., Jones, P.D., & Kennedy, J.J. (2009). Identifying signatures of natural climate variability in time series of global-mean surface temperature: Methodology and Insights. *Journal Climate*, 22, 6120-6141.

Thordarson, T., Miller, D.J., Larsen, G., Self, S., & Sigurdsson, H. (2001). New estimates of sulfur degassing and atmospheric mass-loading by the 934 AD Eldgjá eruption, Iceland. *Journal Volcanic Geothermal Research,* 108, 33–54.

Toohey, M., Krüger, K., Sigl, M., Stordal, F., & Svensen H.H. (2016). *Climatic Change*, 136, 401-412. doi:10.1007/s10584-016-1648-7

Torsvik, T.H., & Trench, A. (1991). The Ordovician history of the Iapetus Ocean in Britain: New palaeomagnetic constraints. *Journal Geological Society London*, 148, 423-425.

Torsvik, T.H., & Cocks, L.R.M. (2017). Earth History and Palaeogeography. Cambridge University Press.

Torsvik, T.H., & Domeier, M. (2017). Correspondence: Numerical modelling of the PERM anomaly and the Emeishan Large Igneous Province. *Nature Communications,* 8. doi:10.1038/s41467-017-00125-2.

Torsvik, T. H. et al. (2001). Late Cretaceous India-Madagascar fit and timing of break-up related magmatism. *Terra Nova*, 12, 220–224.

Torsvik, T.H., Steinberger, B., Cocks, L.R.M. & Burke, K. (2008a). Longitude: Linking Earth's ancient surface to its deep interior. *Earth Planetary Science Letters*, 276, 273-283.

Torsvik, T.H., & Rehnström, E.F. (2003). The Tornquist Sea and Baltica-Avalonia docking. *Tectonophysics*, 362, 67–82.

Torsvik, T.H., & Cocks, L.R.M. (2004). Earth geography from 400 to 250 million years: a palaeomagnetic, faunal and facies review. *Journal of the Geological Society London*, 161, 555-572

Torsvik, T.H., Smethurst, M.A., Burke, K., & Steinberger, B. (2008*b*). Long term stability in Deep Mantle structure: Evidence from the ca. 300 Ma Skagerrak-Centered Large Igneous Province (the SCLIP). *Earth and Planetary Science Letters*, 267, 444–452. doi:10.1016/j.epsl.2007.12.004.

Torsvik, T. H., Steinberger, B., Gurnis, M., & Gaina, C. (2010b). Plate tectonics and net lithosphere rotation over the past 150 My. *Earth Planetary Science Letters*, 291, 106–112.

Torsvik, T.H., Smethurst, M.A., Burke, K., & Steinberger, B. (2006). Large Igneous Provinces generated from the margins of the Large Low-Velocity Provinces in the deep mantle. *Geophysical Journal International*, 167, 1447–1460. doi:10. 1111/j.1365-246X.2006.03158.x

Torsvik, T.H., Rousse, S., Labails, C., & Smethurst, M.A. (2009). A new scheme for the opening of the South Atlantic Ocean and dissection of an Aptian Salt Basin. *Geophysical Journal International*, 177, 1315-1333.

Torsvik, T.H., Burke, K., Steinberger, B., Webb, S.J., & Ashwal, L.D. (2010a). Diamonds sampled by plumes from the core–mantle boundary. *Nature*, 466, 352–355. doi:10.1038/nature09216

Torsvik, T. H., Van der Voo, R., Preeden, U., Mac Niocaill, C., Steinberger, B., Doubrovine, P.V., van Hinsbergen, D.J.J., Domeier, M., Gaina, C., Tovher, E., Meert, J.G., McCausland, P.J., Cocks, L.R.M (2012). Phanerozoic polar wander, paleogeography and dynamics. *Earth-Science Reviews*, 114, 325–368.

Torsvik, T.H., van der Voo, R., Doubrovine, P.V., Burke, K., Steinberger, B., Ashwal, L.D., et al. (2014). Deep mantle structure as a reference frame for movements in and on the Earth. *Proceedings of the National Academy of Sciences USA*, 111 (24): 8735–8740 doi:10.1073/pnas.1318135111.

Torsvik, T. H., Amundsen, H.E.F., Trønnes, R.G., Doubrovine, P.V., Gaina, C., Kusznir, N., Steinberger, B., Corfu, F., Ashwal, L.D., Griffin, W.L., Werner, S.C., Jamtveit, B. (2015). Continental crust beneath southeast Iceland. *Proceedings of the National Academy of Science USA,* 112, E1818–E1827.

Torsvik, T.H., Steinberger, B., Ashwal, L.D., Doubrovine, P.V., & Trønnes, R.G. (2016). Earth evolution and dynamics – a tribute to Kevin Burke. *Canadian Journal Earth Sciences*, 53 (11), 1073–1087. https://doi.org/10.1139/cjes-2015-0228.

Torsvik, T.H., Steinberger, B., Shephard, G.E., Doubrovine, P.V., Domeier, M., Gaina, C., Conrad, C. & Sager, W.W. (2019). Pacific-Panthalassic reconstructions: Overview, errata and the way forward. *Geochemistry, Geophysics, Geosystems* (in review).

Trønnes, R.G., Baron, M.A., Eigenmann, K.R., Guren, M.G., Heyn, B.H., Løken, A. & Mohn, C.E. (2019). Review: Core formation, mantle differentiation and core-mantle interaction within Earth and the terrestrial planets. Tectonophysics. doi:10.1016/j.tecto.2018.10.021

Ukstins Peate, I., & Bryan, S.E. (2008). Re-evaluating plume-induced uplift in the Emeishan large igneous province. *Nature Geoscience*, 1, 625-629. doi:10.1038/ngeo281.

Vasilev, Y.R., Zolotukhin, V.V., Feoktistov, G.D., & Prusskaya, S.N. (2000) Evaluation of the volumes and genesis of Permo-Triassic trap magmatism on the Siberian Platform. *Geol. Geofiz.*, 41 (2000), pp. 1696-1705. (in Russian)

van der Meer, D., Spakman, W., van Hinsbergen, D.J.J., Amaru, M.L., & Torsvik, T.H. (2010). Absolute plate motions since the Permian interred from lower mantle subduction remnants. *Nature Geosciences, 3, 36-40.* doi:10.1038/NGEO708.

van der Meer, D.G, Zeebe, R., van Hinsbergen, D.J.J., Sluijs, A., Spakman, W., & Torsvik, T.H. (2014). Plate tectonic controls on atmospheric CO_2 levels since the Triassic. *Proceedings of the National Academy of Sciences USA*. DOI 10.1073/pnas.1315657111.

van der Meer, D.G., van Hinsbergen, D.J.J. & Spakman, W. (2018). Atlas of the Underworld: subduction remnants in the mantle, their sinking history, and a new outlook on lower mantle viscosity. *Tectonophysics*, 723, 309-448.

Visscher, H., Looy, C.V., Collinson, M.E., Brinkhuis, H., Cittert, J., Kurschner, W.M., et al., (2004). Environmental mutagenesis during the end-Permian ecological crisis. *Proceedings of the National Academy of Sciences USA*, 101, 12952–12956.

Vogt, P.R. (1972). Evidence for global synchronism in mantle plume convection, and possible significance for geology. *Nature*, 240, 338-342.

Vrielynck, B., & Bouysse, P. (2003). The Changing Face of the Earth. The Break-Up of Pangaea and Continental Drift over the Past 250 million Years in Ten Steps. Earth Sciences Series. *UNESCO Publishing/Commission* for the Geological Map of the World (CGMW).

Walker, J.C.G., Hays, P.B., & Kasting, J.F. (1981). A negative feedback mechanism for the long-term stabilization of Earth's surface temperature. *Journal of Geophysical Research,* 86, 9776–9782.

Wignall, P.B. (2001). Large igneous provinces and mass extinctions. *Earth Science Reviews*, 53, 1-33.

Wilson, J.T. (1963). A possible origin of the Hawaiian islands. *Canadian Journal of Physics*, 41, 863–870. doi:10.1139/p63-094.

Worsley, T.R. & Kidder D.L. (1991). First-order coupling of paleogeography and CO_2, with global surface temperature and its latitudinal contrast. *Geology*, 19, 1161-1164.

Wyllie, P.J. (1980). The origin of kimberlites. *Journal of Geophysical Research*, 85, 6902–6910.

Zachos, J., Pagani, M., Sloan, L., Thomas, E., & Billups, K. (2001). Trends, rhythms, and aberrations in global climate 65 Ma to present. *Science*, 292, 686-693.

Zhang, N., Zhong, S.J., Leng, W., & Li, Z.X. (2010). A model for the evolution of the Earth's mantle structure since the Early Paleozoic. *Journal of Geophysical Research: Solid Earth*, 115: B06401. doi:10.1029/2009JB006896.

Zhong, S., & Rudolph, M.L. (2015). On the temporal evolution of long-wavelength mantle structure of the earth since the early Paleozoic. *Geochemistry Geophysics Geosystems*, 16, 1599–1615.

Zhong, S., Zhang, N., Li, Z.-X., & Roberts, J.H. (2007). Supercontinent cycles, true polar wander, and very long-wavelength mantle convection. *Earth and Planetary Science Letters*, 261, 551–564.

Zurevinski, S.E., Heaman, L.M., & Creaser, R.A. (2011). The origin of Triassic/Jurassic kimberlite magmatism, Canada: Two mantle sources revealed from the Sr–Nd isotopic composition of groundmass perovskite. *Geochemistry, Geophysics, Geosystems*, 12, Q09005. doi:10.1029/2011GC003659

Appendix 1: Computing plume ascent time

Both for the plume conduit and the plume head, lateral advection is computed from the ambient mantle flow field. Radial motion of plume conduit elements is computed as the sum of ambient mantle flow and rising speed, whereas for the plume head, buoyant rising is dominant and the ambient vertical flow component is disregarded. Also, if the contribution of ambient flow on plume head rising were considered, it would not be possible to prescribe total ascent time, and hence match the hotspot age (Table 1) for a specified time when the plume head starts rising from the lowermost mantle, as it could only be determined after the modelling. To compute mantle flow, mantle density structure is derived from a seismic tomography model. Here we use *s10mean* (Doubrovine *et al.* 2016) but we also report results using *smean* (Becker & Boschi 2002) for comparison. For most of the mantle, we use a thermal scaling of seismic velocity to density anomalies (Model 2 of Steinberger & Calderwood 2006), but we also consider that LLSVPs are probably chemically distinct, by adding a "chemical" density anomaly (1.2%) to those regions below a certain depth (2600 km, i.e. in the lowermost 300 km of the mantle) where the seismic velocity anomaly is more negative than a specified value (-0.9% for *s10mean*, -1% for *smean*). The LLSVPs were outlined in this way because steep horizontal gradients in seismic velocity tend to be most frequent near those values of shear-wave anomaly, and both seismic velocity anomalies themselves and steep horizontal gradients are most pronounced in the lowermost 300 km (Torsvik *et al.* 2006; Burke *et al.* 2008). Adding a chemical density anomaly of 1.2% makes the piles overall slightly negatively buoyant, despite being hotter, approximately consistent with their long-term stability and cross-sectional shape (Mulyukova *et al.* 2015a) and CMB topography constraints (Steinberger & Holme 2008). Regardless of whether this chemical anomaly is added, LLSVPs are overlain by buoyant, rising material. Hence, large-scale flow structure, and inferred plume source locations do not strongly depend on whether or not the chemical anomaly is considered.

In the uppermost 220 km, density anomalies are reduced by a factor 0.5 because strong positive seismic velocity anomalies in the continental lithosphere would otherwise be interpreted as unrealistically strong density anomalies. This simplified treatment is justified because density anomalies in the upper 220 km have almost no effect at all on the results. We use the preferred mantle viscosity model 2b of Steinberger & Calderwood (2006), which features a strong increase of viscosity with depth, from ~3×10^{20} Pas below the lithosphere to nearly 10^{23} Pas in the lower part of the lower mantle. A similar viscosity structure was previously found to yield sufficiently slow hotspot motion compatible with observed tracks (Steinberger & O'Connell, 1998): A rather high viscosity in the lowermost mantle is required

such that mantle flow, and hence advection of plume conduits, is sufficiently slow. A low viscosity just below the lithosphere helps to largely decouple mantle flow from plate motions, which are imposed as boundary conditions to flow, and hence prevents plume conduits from becoming strongly tilted (incompatible with observations) by moving plates. Results strongly depend on which mantle viscosity structure is used (Steinberger & O'Connell 1998), however for those viscosity structures which yield amounts of hotspot motion compatible with observations, and moderate plume conduits tilts typically not exceeding 60°, and which also match other constraints (geoid, heat flux, postglacial rebound), results tend to be overall similar. Hence, we do not vary mantle viscosity here.

Based on the viscosity and density structure, and time-dependent plate motions (Torsvik *et al.* 2010b) prescribed as surface boundary conditions, large-scale mantle flow is computed with the method of Hager & O'Connell (1979, 1981), extended to consider compressibility (Panasyuk *et al.* 1996) and the effect of phase boundary deflection but disregarding latent heat release and absorption at phase boundaries, as this was found to play a minor role (Steinberger 2007). At the core-mantle boundary, we use a free-slip boundary condition, except for spherical harmonic degree-1 toroidal flow (the net rotation component) where we use no-slip, such that it is possible to apply a net rotation of the lithosphere without causing a net rotation in the deep mantle. Radial density structure is adopted from PREM (Dziewonski & Anderson 1981), and a constant gravity 10 m/s^2 is used. The flow field is also used to backward-advect density heterogeneities, which are hence time-dependent. Before 68 Ma, a constant density structure is used, as backward-advection becomes increasingly unreliable further back in time (Steinberger & O'Connell 1998). Considering time-dependence of flow is not crucial, and results remain qualitatively similar even if constant present-day flow is used. To model the motion of the plume conduit we use hotspot ages, buoyancy fluxes and locations as listed Table 1, and with these parameters and viscosity structure, the plume conduit rising speed through the surrounding mantle is computed as in Steinberger *et al.* (2004) based on a modified Stokes formula (Richards & Griffiths 1988). The hotspot ages correspond to the time when the plume reaches the surface. The time when the plume head detaches from the source depth (taken as 2620 km depth, at the top of a low-viscosity D" layer) is accordingly earlier by an amount equal to the plume head rise time.

Table 1 List of 27 hotspots that we analyse (Fig. 5) and which are those considered to be potentially sourced by deep plumes from the core-mantle boundary (French & Romanowicz 2015). We largely adopted hotspot ages, anomalous mass (buoyancy) fluxes and hotspot locations from Steinberger (2000, *Table 1*). For plumes included in Steinberger & Antretter (2006) we adopted locations from Table 1 of that paper (the first one, if several are given). We here use ages 31 Ma for East Africa (Afar), 62 Ma for Iceland and 135 Ma for Tristan, and for Hawaii, Kerguelen, Louisville, Marion, Reunion and Samoa we adopt ages from Steinberger & Antretter (2006), based in part on newer and better age constraints of the associated flood basalts. For Ascension, which is not included in either of these papers, the location (14.3°W, 7.9°S) corresponds to Ascension Island, an age of 20 Ma is inferred from the location of the further one of two seamounts, ~500 km west of the island, and local South America plate motion in a hotspot reference frame (Doubrovine *et al,* 2012). Anomalous mass flux $0.7 \cdot 10^3$kg/s is inferred from averaging over the same sources as in Steinberger (2000).

Hotspot	Long (°)	Lat (°)	Age (Ma)	Anomalous mass flux (10^3kg/s)	Category*
Ascension	-14.3	-7.9	20	0.7	3
Azores	-28.4	38.5	100	1.2	3
Cameroon	9.2	4.2	31	0.5	2
Canary	-18	28	65	1	1
Cape Verde	-24	15	20	1.1	1
Caroline	164	5	80	1.6	2
Comores	43.3	-11.8	63	0.5	1
East Africa (*Afar)*	34	6	31	1.1	1
Easter	-109.3	-27.1	100	2.1	2
Galapagos	-91.5	-0.4	85	1.4	2
Hawaii	-155.3	19.4	120	6.5	1
Hoggar	6	23	20	0.6	3
Iceland	-17	64.4	62	1.2	1
Juan Fernandez	-82	-34	30	1.7	3
Kerguelen	69	-49	118	0.9	2
Louisville	-138.1	-50.9	121	2	2
Macdonald	-140.2	-29	120	3.6	1

Marion *(Crozet)*	37.8	-46.9	182	0.5	3
Marquesas	-138	-11	9	3.9	1
Meteor *(Bouvet)*	1	-52	120	0.5	3
Pitcairn	-129	-25	8	2.5	1
Reunion	55.7	-21.2	65	1.4	2
Samoa	-169.1	-14.1	40	1.6	1
San Felix	-80	-26	30	1.9	3
St Helena	-10	-17	100	0.4	2
Tahiti	-148.1	-17.9	5	4.5	1
Tristan	-11.3	-38.7	135	1	2

*Follows classification of French & Romanowicz (2016): (1) Primary, (2) clearly resolved, and (3) somewhat resolved.

Table 2 Large Igneous Provinces (LIPs, Fig. 4a), eruption latitude with respect to the Earth's spin axis (i.e. paleomagnetic latitude), mass extinctions (1-5), Oceanic Anoxic Events (OAEs; black shaded rows) and carbon-isotope excursion or black shale development not formally classified as OAEs (grey shaded rows; see Fig. 3b-d). Reconstruction of the LIPs with respect to the mantle is shown in Fig. 4b. LIP type: CLIP, continental; OLIP, Oceanic. [1]Peak magmatic activity around 55-56 Ma, near the PETM, and just prior to opening of the Northeast Atlantic (Torsvik *et al.* 2015); [2]Magmatic activity occurred from 92 to 84 Ma with peak magmatic activity around 87 Ma and just a few million year before India/Seychelles drifted off Madagascar (Torsvik *et al.* 2001). [3,4]Uncertain to reconstruct in an absolute reference frame (not reconstructed in Fig. 4b); [5]Ernst (2014) assumed an emplacement age of 130 Ma (oldest known date is 128 Ma) whilst Madrigal et al. (2016) used an initial LIP age of 140 Ma ("magnetic anomaly age") for the main volcanic constructs. [6]Most preserved parts are allochthonous and thus there are considerable reconstruction uncertainties.

Age (Ma)	Large Igneous Province	Eruption Latitude	Mass extinction/Anoxia events	LIP type
15	Columbia River Basalt	46.8°N		CLIP
31	Afar	4.2°N		CLIP
56			PETM	
62	North Atlantic Igneous Province[1]	52.9°N		CLIP
66	Deccan	22.7°S	#5	CLIP
73	Sierra Leone Rise	1.4°S		OLIP
87	Madagascar[2]	46°S		CLIP/OLIP
90	Caribbean[3]	~ 0°N		CLIP/OLIP
94			OAE2	
95	Broken Ridge	49.3°S		OLIP
100	Hess Rise	4.3°N		OLIP
100	Central Kerguelen	48.7°S		OLIP
100	Agulhas Plateau	55.2°S		OLIP
111	Nauru Basin	20°S	OAE1b	OLIP
114	South Kerguelen	55.3°S		OLIP
118	Rajmahal	46.1°S		CLIP
121			OAE1a	
123	Ontong Java Nui mega-LIP (Ontong Java, Manihiki & Hikurango Plateaus)	31.4°S		OLIP
124	High Arctic LIP[4]	~ 60°N		CLIP/OLIP
124	Wallaby Plateau	47.2°S		OLIP
125	Maud Rise	49.9°S		OLIP
132	Bunbury	62.7°S		CLIP
134	Paraná-Etendeka	27.7°S		CLIP
135	Magellan Rise	18.6°S		OLIP
136	Gascoyne	54.5°S		OLIP
140	Mid-Pacific Mountains[5]	6.1°S		OLPI
144	Shatsky Rise	7°N		OLIP
155	Argo Margin	41.3°S		OLIP
183	Karoo-Ferrar	39.5°S	OAE	CLIP
201	Central Atlantic Magmatic Province	2.8°N	#4	CLIP
252	Siberian Traps	62.4°N	#3	CLIP

260	Emeishan	5.1°S		CLIP
285	Panjal Traps (Tethyan Plume)[#6]	46.2°S		CLIP
297	Skagerrak Centred LIP	11.3°N		CLIP
360	Yakutsk	36.6°N	**#2**	CLIP
372			OAE	
400	Altay-Sayan	30.9°N		CLIP
470				
445			**#1**	
501			OAE	
510	Kalkarindji	6.5°N		CLIP
517			OAE	

Table 3 Estimated subduction flux for the past 400 Myrs that we use to define the time-dependent (normalized) f_{SR} parameter (i.e. 1.00 = today) in the GEOCARBSULF model (Fig. 12c). Subduction flux calculated dynamically from the Paleozoic full-plate model of Domeier & Torsvik (2014) and a revised Mesozoic-Cenozoic full-plate model (250-0 Ma; Torsvik *et al.* 2019), which is originally based on Matthews *et al.* (2016). Using the latest GEOCARBSULF model (Royer et al. 2014) but with our revised estimates for plate tectonic degassing (f_{SR}) we have modelled the atmospheric CO_2 for the past 400 Myrs with two different weathering models (WM). The GEOCARB R code was ran with the *"resampleN"* parameter set to 1 and the two different weathering models are selected by the *"Godderis"* parameter set to TRUE (WM-1; Godderis *et al.* 2012) or FALSE (WM-2; Berner 2006).The model code and original input files from Royer et al. (2014) available at:
https://figshare.com/articles/code_to_run_GEOCARBSULF_model/902207

			WM-1	WM-2
Age	**Subduction flux**	f_{SR}	**CO$_2$**	**CO$_2$**
(Ma)	(km^2/year)		(ppm)	(ppm)
400	5.56	1.92	3825	2680.6
390	4.83	1.67	1711	1331.6
380	4.30	1.48	1798	1551.0
370	5.63	1.94	1621	1539.7
360	6.42	2.21	1506	1398.6
350	5.52	1.90	485	415.4
340	5.21	1.80	709	545.1
330	4.69	1.62	460	407.9
320	4.09	1.41	439	393.3
310	3.90	1.34	411	370.4
300	4.02	1.39	401	368.8
290	4.27	1.47	500	418.9
280	4.30	1.48	552	410.2
270	4.38	1.51	467	332.9
260	4.88	1.68	575	362.9
250	3.38	1.17	1872	565.9
240	3.70	1.28	1966	517.8
230	3.24	1.12	1436	445.0
220	3.20	1.10	908	318.7
210	3.38	1.17	836	437.7
200	3.26	1.12	444	354.9
190	2.84	0.98	429	388.1
180	3.25	1.12	353	388.3
170	3.54	1.22	275	294.6
160	3.83	1.32	314	339.6
150	4.34	1.50	417	454.5
140	5.41	1.87	733	852.3
130	6.85	2.36	879	1191.7
120	5.45	1.88	436	631.2

110	5.14	1.77	373	652.9
100	4.02	1.39	232	486.5
90	4.80	1.66	244	659.0
80	4.20	1.45	211	540.1
70	4.60	1.59	255	578.5
60	4.48	1.54	301	477.8
50	3.68	1.27	241	279.9
40	3.48	1.20	227	246.1
30	3.84	1.32	261	265.2
20	3.38	1.17	279	263.9
10	3.12	1.08	295	266.1
0	2.90	1.00	270	243.0

FIGURES
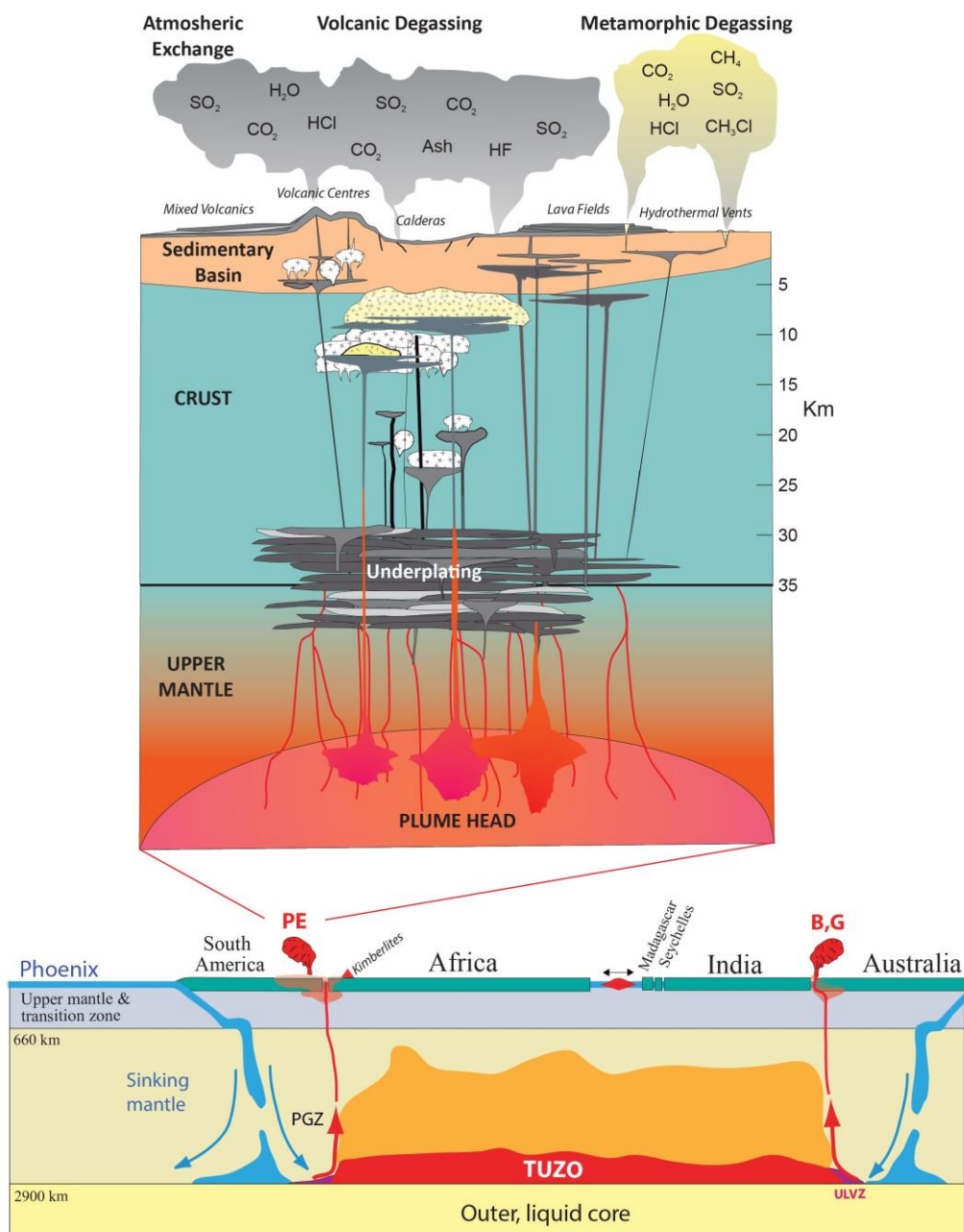
Figure 1. The dynamic exchanges from the core to atmosphere. **(a)** The internal pluming system, eruption and degassing during LIP emplacement (adapted from Bryan *et al.* 2010; Jerram & Bryan 2015; Jerram *et al.* 2018). Melt can be emplaced at various levels within the crust and the mix of volcanic and metamorphic degassing exchanges gases into the Earth's atmosphere (e.g. Svensen & Jamtveit 2010; Jones *et al.* 2016). **(b)** A cartoon profile approximately through the reconstructed Paraná-Etendeka (PE) LIP, North Madagascar-Seychelles, India and Australia at ~135 Ma (after Svensen *et al.* 2018; Torsvik 2018). The slabs that influenced the formation of plumes sourcing the Paraná-Etendeka LIP, and contemporaneous kimberlites in South Africa and Namibia, were probably linked to an old subduction zone along the western margin of South America. The South Atlantic opened shortly after the Paraná-Etendeka LIP. Conversely, the Gascoyne (G) and Bunbury (B) LIPs were linked to old subduction systems along eastern Australia. Earth today is a degree-2 planet dominated by the two antipodal large low-shear-wave velocity provinces in the lower mantle (Figs. 4b, 5) beneath Africa (TUZO) and the Pacific (JASON), which are warmer but probably also denser and stiffer than the ambient mantle in its lowermost few hundred kilometres. Here we only show TUZO, and the orange colour is shown to indicate that the area above TUZO is also warmer than the background mantle. PGZ, plume generation zone; ULVZ, Ultra Low Velocity Zone.
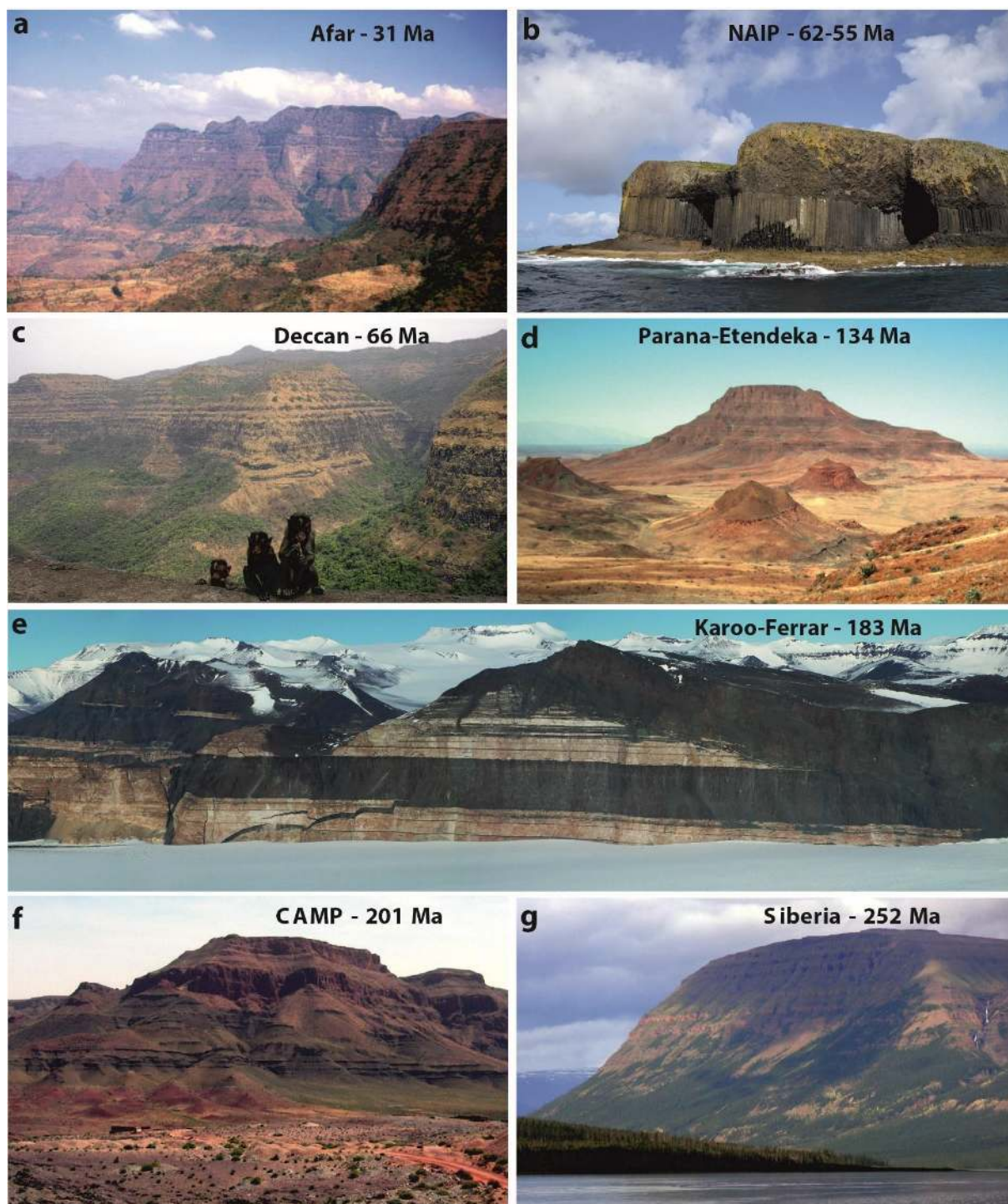
Figure 2. The expression of LIPs on the Earth's surface with key examples through time. **(a)** Ethiopian plateau, Afar (Ethiopia-Yemen province). **(b)** Fingal's cave, North Atlantic Igneous Province (NAIP), Scotland. **(c)** Deccan Traps, India. **(d)** Etendeka lava sequences in Namibia, Paraná-Etendeka Province. **(e)** Giant sill complexes in Antarctica, Karoo-Ferrar Province. **(f)** Rare lava flow examples in Morocco, Central Atlantic Magmatic Province (CAMP). **(g)** Siberian Traps in Russia. Panel f photograph courtesy of Sara Callegaro. All other photographs by Dougal Jerram.
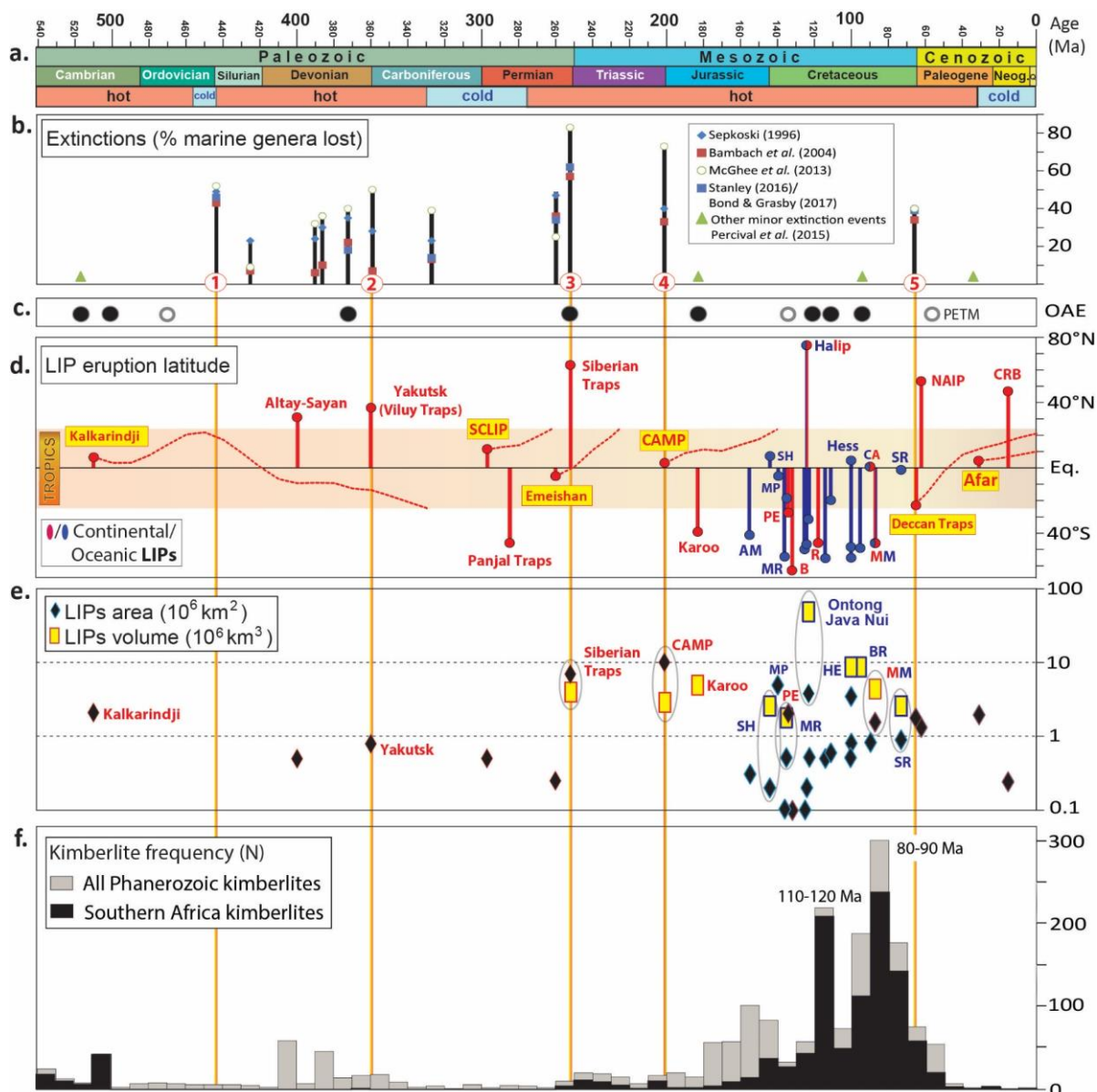
Figure 3 (a) Phanerozoic timescale with greenhouse (hot) *versus* icehouse (cold) conditions (Torsvik & Cocks 2017). **(b)** Major extinction events (% marine genera lost; see Bond & Grasby 2017) and other minor extinction events (Percival *et al.* 2015). The "Big Five" mass extinctions are labelled 1 to 5 (see also Table 2). **(c)** Ocean Anoxic Events (OAEs, black filled circles) and carbon-isotope excursion/or black shale development not formally classified as OAEs (open white circles, e.g. PETM, Paleocene-Eocene thermal maximum at ~56 Ma). (**d**) LIP eruption latitudes calculated from paleomagnetic data (i.e. relative to the spin-axis) for the past 510 Myrs. We have reconstructed the estimated latitudinal centres through time (red dashed lines) for those LIPs that remained within the tropics for considerable times. Note that CAMP (Central Atlantic Magmatic Province) is reconstructed for North America and CAMP volcanics in NW Africa and South America will essentially stay within the tropics until present times. AM, Argo Margin; B, Bunbury; BR, Broken Ridge; CA, Caribbean; CAMP, Central Atlantic Magmatic Province; CRB, Columbia River Basalt; HALIP, High Arctic LIP; HE, Hess Rise; MR, Maud Rise; MR, Mid-Pacific Mountains; MM, Madagascar-Marion; NAIP, North Atlantic Igneous Province; PE, Paraná-Etendeka; SCLIP, Skagerrak Centred LIP; SH, Shatsky Rise; SR, Sierra Leone Rise; R, Rajmahal. **(e)** Estimated area extent and volumes for Phanerozoic LIPs (logarithmic scale; updated from Ernst & Buchan 2001; Ernst 2014). **(f)** Kimberlite frequency plot (N=1918) for the Phanerozoic (grey bars in 10 Myr bins). Also shown the frequency distribution separately for southern African kimberlites (N=867) as black bars. Globally, two main peaks are identified for the Phanerozoic – between 80-90 Ma and 110-120 Ma – but both Cretaceous peaks are dominated by kimberlite eruptions in southern Africa. Ages based on a combination of *in-house* CEED-industry sources (Torsvik *et al.* 2010a; 2014; Torsvik & Cocks 2017) and Tappe *et al.* (2018; only kimberlites and not related rocks also listed in this compilation; e.g. lamprophyres).
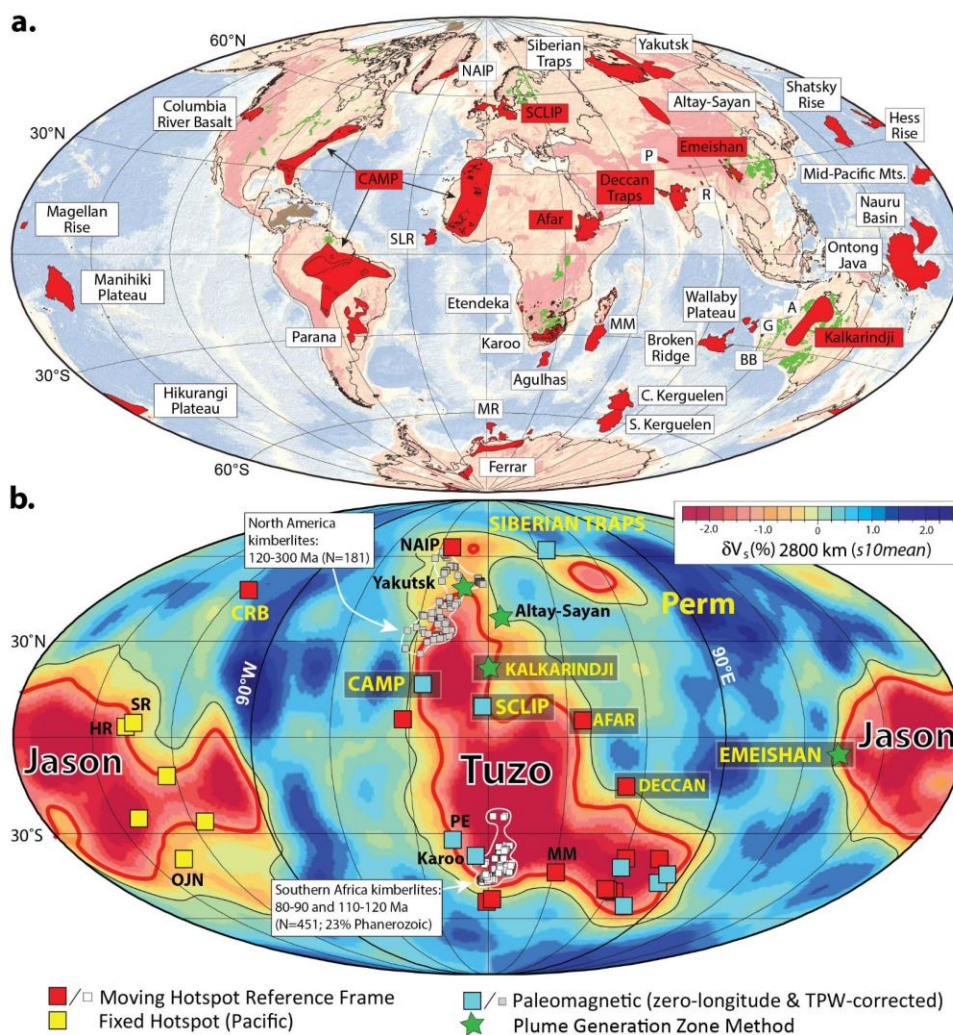
Figure 4 (a) The location of 32 Phanerozoic large igneous provinces (LIPs; 15 to 510 Myr old) which we can reconstruct with varying confidence back to their eruption time (panel b). These are shown with red polygon fills whilst two others that we do not reconstruct (Caribbean and the High Arctic LIPs) are shown with brown polygon fills. Precambrian/Early Cambrian rocks argued to be LIP-related are shown with green polygon fills (Ernst 2014). The areal extent of the Central Atlantic Magmatic Province (CAMP) is liberal in the inclusion of ~201 Myr basalts, sills and dykes. **(b)** Reconstructed estimated LIP centres (based on panel **a**) using four different reconstruction methods. After 83.5 Ma we use a global moving hotspot frame. In the Indo-Atlantic realm this is extended by a moving hotspot frame to 120 Ma (red squared symbols) and a paleomagnetic frame corrected for true polar wander 120-320 Ma (blue squared symbols). The Pacific-Panthalassic can only be extended from 83.5 Ma to ~150 Ma with a fixed hotspot frame (yellow squared symbols; Torsvik et al. 2019). Before Pangea we can use the plume generation zone (PGZ) method (green triangles) (see text for details). Reconstructed LIPs are draped on the *s10mean* tomography model (2800 km depth; Doubrovine *et al.* 2016). The lowermost mantle is dominated by two antipodal large low shear-wave velocity provinces (LLSVPs; Garnero et al. 2007) beneath Africa (TUZO) and the Pacific (JASON). Most LIPs are formed near their margins – the plume generation zones (PGZs) – which are approximated by the 0.9% slow contour (thick red line) in *s10mean*. The Columbia River Basalt (CRB) is an exception as it erupted above an area of high shear-wave velocities (blue regions) in the lowermost mantle and the Siberian Traps may overlie a smaller and perhaps separate anomaly, named Perm (Lekic et al. 2012). Abbreviated LIPs include: A, Argo; BB, Bunbury; CAMP, Central Atlantic Magmatic Province; G, Gascoyne; HR, Hess Rise; MM, Madagascar-Marion; MR, Maud Rise; NAIP, North Atlantic Igneous Province; OJN, Ontong Java Nui; P, Panjal; PE, Parana-Etendeka; R, Rajmahal; SCLIP, Skagerrak Centred LIP; SLR, Sierra Leone Rise; SR, Shatsky Rise. We have highlighted six continental LIPs that erupted at low latitudes (e.g. CAMP). We have also included two examples of reconstructed kimberlites, *(i)* reconstruction of 451 Southern African (South Africa, Botswana, Angola & Lesotho) kimberlites between 80-90 Ma and 110-120 Ma (dominating the two global kimberlite frequency peaks in Fig. 3f), and *(ii)* reconstruction of 181 North American (USA, Canada) kimberlites with ages from 120 to 300 Ma.
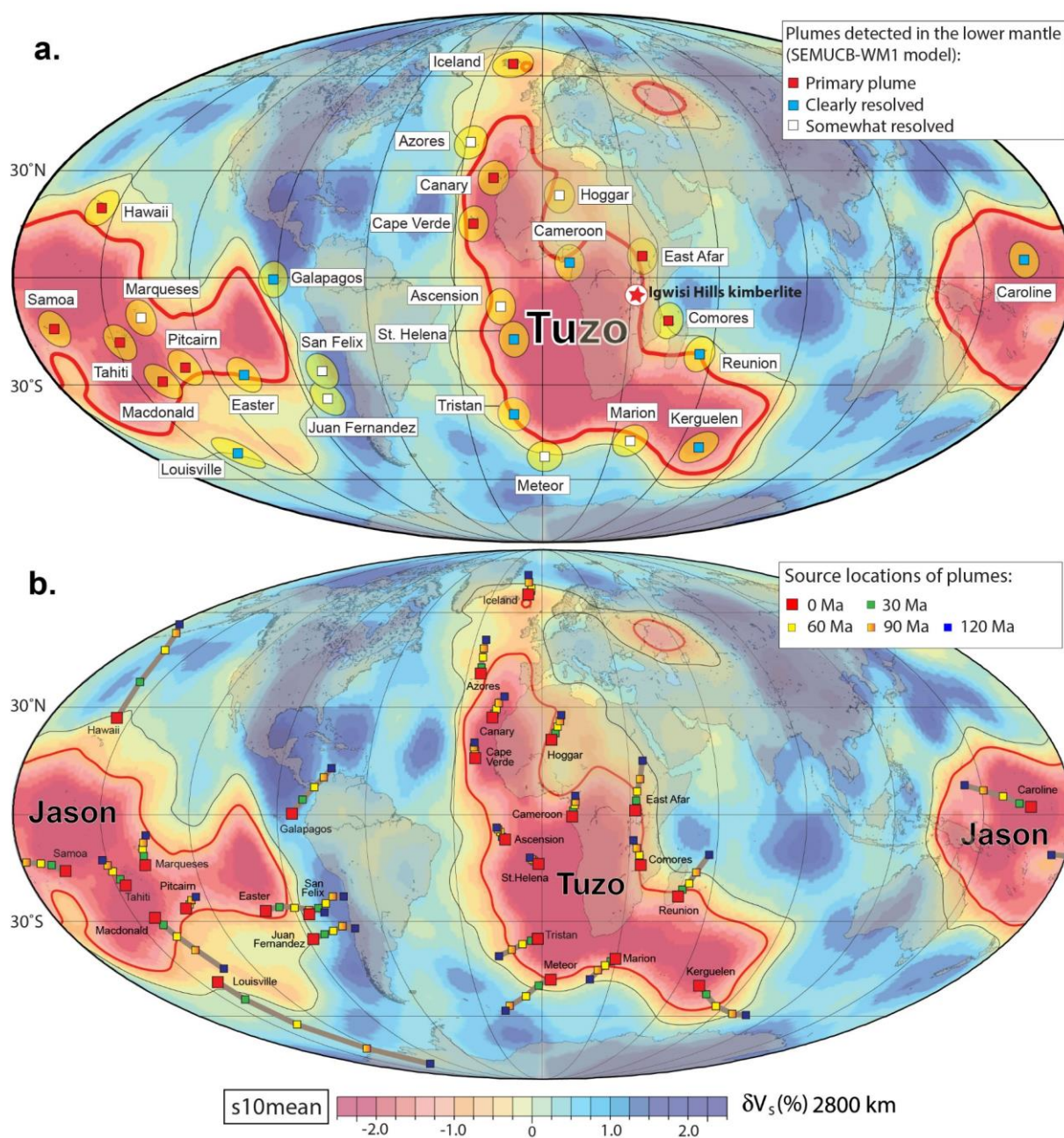
Figure 5 (a) Seismic tomographic *s10mean* model (δV$_S$%) at 2800 km depth (Doubrovine *et al.* 2016). The thick red line is the 0.9% slow contour and approximates the plume generation zones (PGZs; largest horizontal gradients in *s10mean*). The thin black lines are the zero contours. The location of 27 inferred deep-rooted plumes (French & Romanowicz 2015) are shown with 5° ovals which are close to the average great-circle distance to the PGZ (5.8 ± 4.4°). We also show the location of the youngest kimberlite on Earth (Igwisi Hills kimberlite in Tanzania), only 12,000 years and can therefore be shown on the map without reconstructing it. **(b)** Computed plume source locations in the lowermost mantle for plume head rise times 0-120 Myr, for time-dependent mantle flow based on *s10mean* tomography, and considering the LLSVPs to be chemically dense piles (see text and Appendix 1).
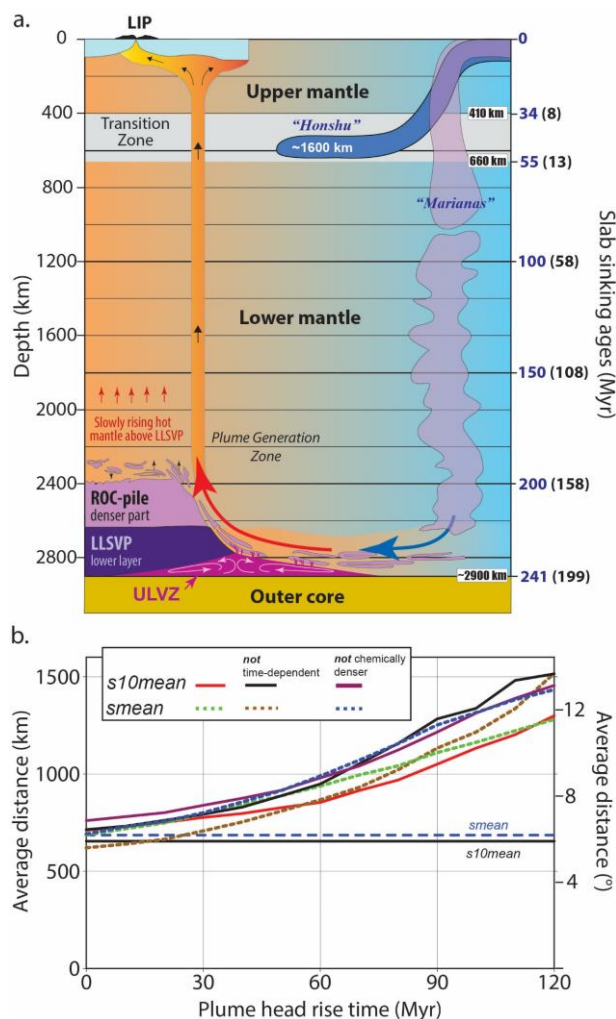
Figure 6 (a) Schematic representations of present day sinking slabs (based on fast seismic anomalies; Goes *et al.* 2016) in the Northwest and West Pacific illustrating a slab that has flattened and stagnated (Honshu with a flattened slab length of ~1600 km) and the Marianas slab that directly penetrated the base of the transition zone (660 km). Interpretation of lower mantle slab ages therefore critically depends on their upper mantle history: Black coloured sinking ages (in brackets) assume sinking rates of 5 cm/yr in the upper mantle and 1.2 cm/yr in the lower mantle, and approximately represent slabs directly penetrating the transition zone and then sinking slower in the lower mantle. Blue coloured slab sinking ages assume constant sinking rates (1.2 cm/yr) for the entire mantle; this is unrealistically low for the upper mantle but can be regarded as a proxy for slabs with a long residence time in the transition zone (tens of million years). This time could be longer if basaltic materials (ROC; recycled oceanic crust) first get incorporated into the thermochemical piles (LLSVPs), before they become entrained into plumes. The ROC (recycled oceanic crust) stockpile, indicated here, and forming the upper parts of the LLSVPs, might be continuously replenished in relatively stagnant regions between plumes, concurrently with erosion near plumes rooted along the LLSVP margins (Torsvik *et al.* 2016; Trønnes *et al.* 2019). Some plumes may directly penetrate the lithosphere and in the process create new plate boundaries, but "upside-down drainage" (Sleep 1997) provides an explanation of how many LIPs may have erupted into pre-existing rifts or active spreading centres. This is exemplified here by an oceanic LIP that initially may have erupted into an active spreading ridge. **(b)** Average distances of plume source locations (great-circle distances in km or degrees) from the plume generation zone (PGZ). Apart from the reference case (red line, corresponding to Fig. 5b), based on *s10mean* tomographic model (Doubrovine *et al.* 2016), we also include results with constant (not time-dependent) flow (black line), results without considering that the LLSVPs (TUZO and JASON) are chemically denser (violet line) and results based on the *smean* (Becker & Boschi 2002) tomography model, both for computing mantle flow and plume sources (see Appendix 1), and for defining the PGZ (stippled green, brown and blue lines corresponding to red, black and violet lines, respectively). Horizontal lines show the average distance of surface hotspot locations, for comparison, from PGZ's based on *s10mean* (black) and *smean* (stippled blue; -1% contour).
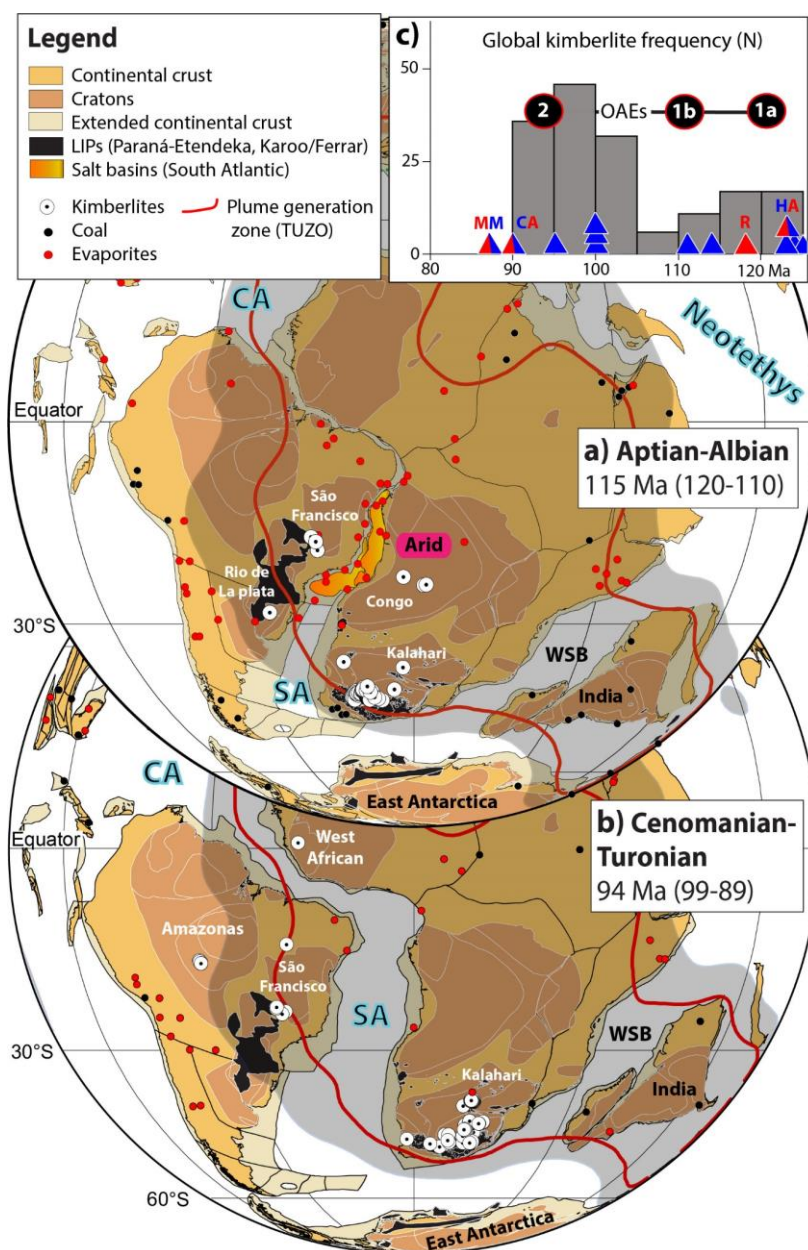
Figure 7 (a) Cretaceous (Aptian-Albian) paleomagnetic reconstruction (~115 Ma) with occurrences of kimberlite (large white shaded circles with a central black dot), evaporite (red shaded circles and salt basins in the South Atlantic; Torsvik *et al.* 2009) and coal (black/white shaded circles). Symbols may represent multiple occurrences (e.g. 213 kimberlite pipes averaging to 118 ± 2 Ma are found within the Kalahari and Congo cratons). For comparison with the areal extent of kimberlite pipes we show the LIP outlines of Paraná-Etendeka (Brazil, Namibia) and Karoo-Ferrar in Southern Africa and East Antarctica. Precambrian craton outlines after Gubanov & Mooney (2009). CA, Central Atlantic (early opening at around 195 Ma shortly after CAMP erupted); SA, South Atlantic (seafloor spreading south of Walvis Ridge started at ~130 Ma and shortly after Parana-Etendeka LIP erupted). WSB, West Somalian Basin (early opening at around 170 Ma and soon after Karoo-Ferrar LIP; Gaina *et al.* 2013). **(b)** Cretaceous (Cenomanian-Turonian) paleomagnetic reconstruction (~94 Ma) with occurrences of kimberlite (127 kimberlite pipes in Kalahari craton between 89 and 99 Ma), evaporite and coal. We also show the plume generation zones (red thick lines) which have been counter-rotated +10° (panel a) and +4° (panel b) around 0°N and 11°E to account for true polar wander at these times. **(c)** Global distribution of kimberlites (5 Myr bins) but only the most reliable dated kimberlites (U/Pb zircon and perovskite age) between 80 and 125 Ma (N=172). The majority of the kimberlites are from Southern Africa and many statistically overlap with the Cretaceous Oceanic anoxia events OAE1 (sub-divided into 1a and 1b) and OAE2. This is also the time of the most widespread occurrences of LIPs (blue and red triangles), mostly oceanic LIPs (blue triangles) except for the small Rajmahal (R) LIP in India, and the partly continental/oceanic High Arctic (HA), Caribbean (CA) and Madagascar (MM) LIPs which mostly erupted before or after these Cretaceous OAEs events.
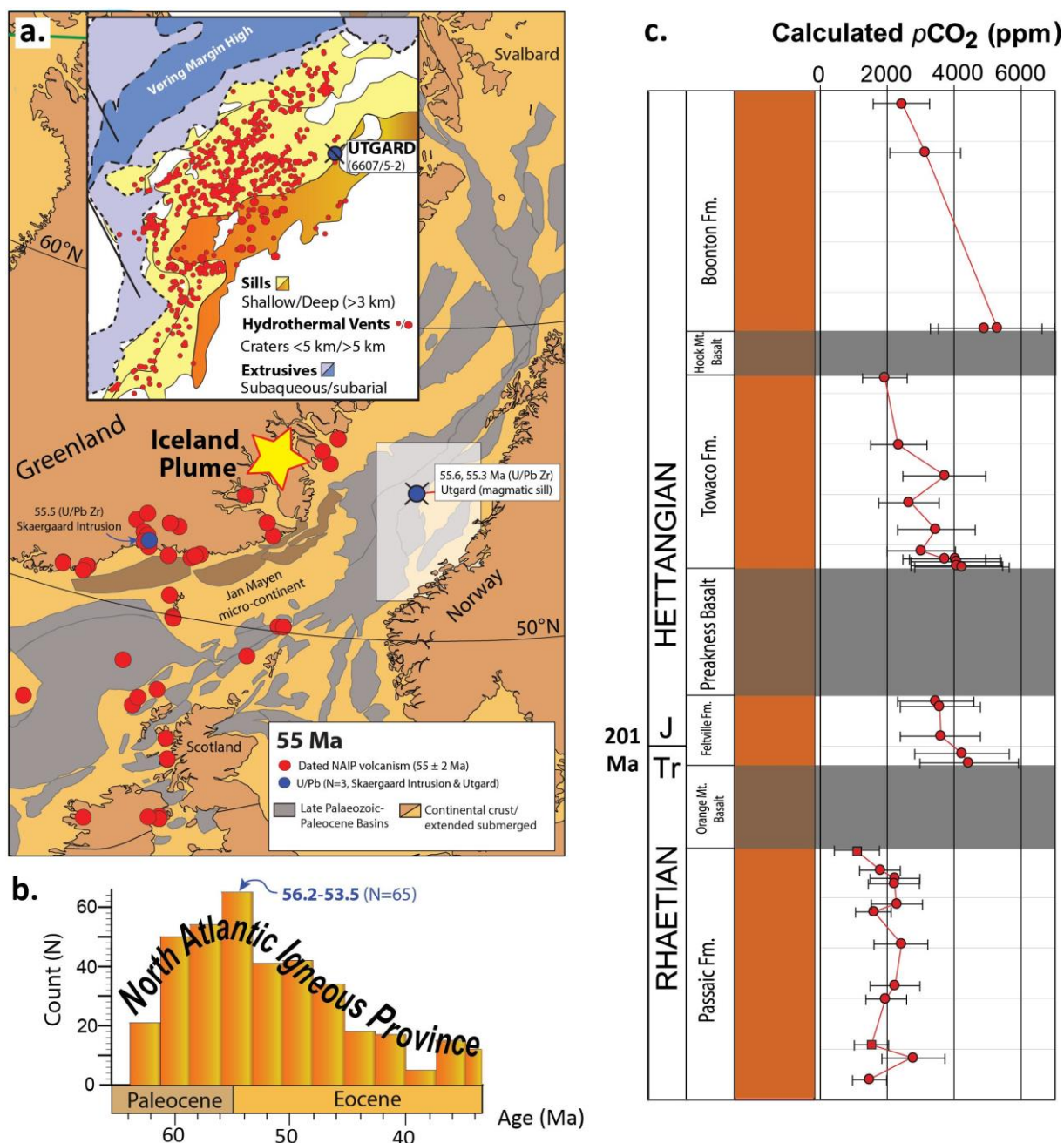
Figure 8 (a) Reconstruction of the Northeast Atlantic at 55 ± 2 Ma with the distribution of dated onshore and offshore sample locations (red/blue filled circles) for the North Atlantic Igneous Province (NAIP), the location of the Iceland plume (yellow star) with respect to Greenland (Torsvik *et al.* 2015; Torsvik & Cocks 2017), and rift basins developed from the Late Paleozoic to the Paleocene (Faleide *et al.* 2010). Peak NAIP volcanic activity overlapped with the Paleocene Eocene Thermal Maximum (PETM) at ~56 Ma. The *inset* map demonstrates the extensive sill and hydrothermal vent complexes in the Vøring Basin offshore Norway (see white box in main map), and location of the Utgard borehole where magmatic sills intruding organic-rich sediments are dated to 55.6 and 55.3 Ma (U/Pb Zircon; Svensen *et al.* 2010). **(b)** Histogram of 383 isotope ages from NAIP (Torsvik et al. 2015), mainly $^{40}Ar/^{39}Ar$ and K/Ar ages, with 3% high-precision U/Pb ages (Torsvik & Cocks 2017), 62.6 Ma (Antrim basalt in Ireland) to 55.5 Ma (Skaergaard intrusion, East Greenland), 55.6 and 56.3 Ma (magmatic sills in the Vøring area, offshore mid-Norway). **(c)** Stratigraphy and lithology of the upper Newark Basin, Eastern North America (part of the ~201 Ma Central Atlantic Magmatic Province, CAMP) and calculated pCO_2 from stable isotopic values of pedogenic carbonates (Schaller *et al.* 2011). Increased pCO_2 values above each volcanic unit (grey rectangles) interpreted as a response to magmatic activity whilst decreases in pCO_2 after each magmatic episode are argued to reflect rapid consumption of atmospheric CO_2 by silicate weathering of fresh CAMP volcanics.
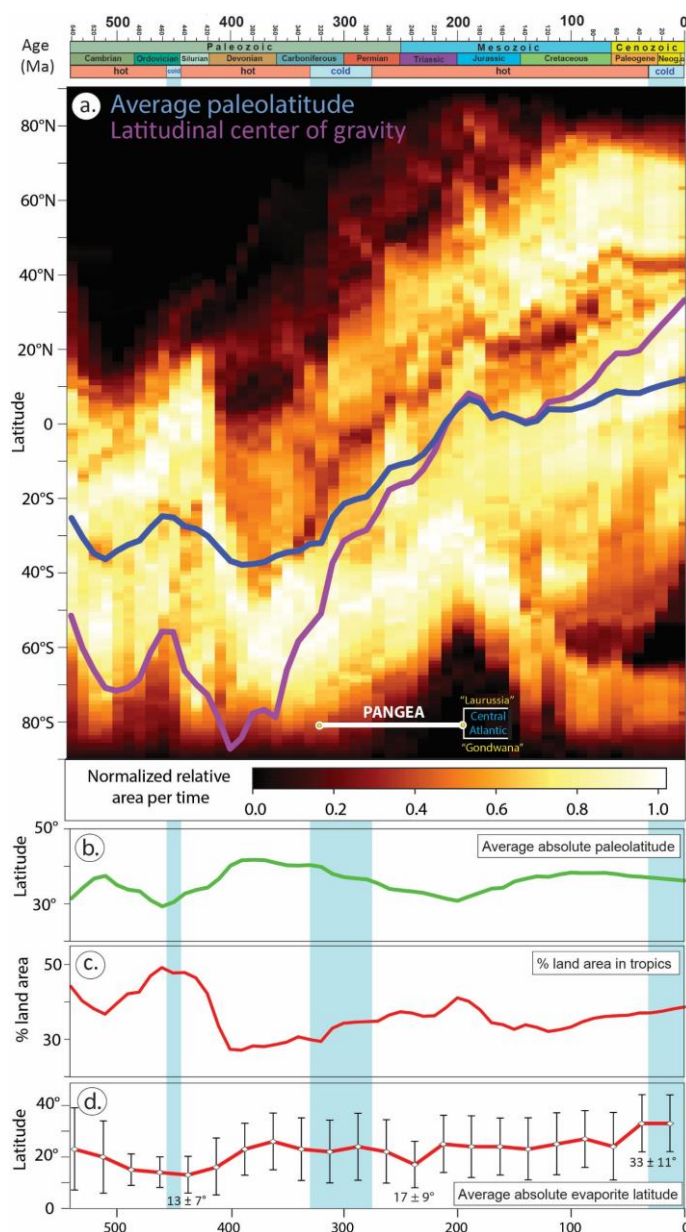
Figure 9 Phanerozoic timescale with greenhouse (hot) *versus* icehouse (cold) conditions and **(a)** Continental paleolatitude through the Phanerozoic, according to continental polygons and total reconstruction poles taken from Torsvik *et al.* (2014). Only continental blocks that are defined (both as a polygon and by rotation history) through the entire 541-0 Ma interval are used, which amounts to a constant area of ~27% of Earth's surface. The distribution of continental paleolatitudes was calculated in 10 Myr steps across the Phanerozoic, wherein for each step the relative area in each 1° latitudinal band (90°S to 90°N) was determined and normalized such that the band with the largest absolute area was set equal to 1. The "heat-map" shows how the latitudinal distribution of continental area changes as a function of time according to this definition. Note that the South Polar region remains dark even though it was occupied by continents at several times in the past (including at present-day), because the area of the polar regions is small compared to the area of lower latitudes (the pole itself has no area); so the heat-map does not necessarily show the position of the continents directly, but how their area is latitudinally distributed. The blue curve shows the average continental paleolatitude, weighted by area. The purple curve shows the latitude component of the 3D continental 'center of gravity' vector, which is the vector sum of area-weighted continental position vectors (defined by both latitude and longitude). The latitude component of this vector can reach much higher latitudes than the average latitude weighted by area (e.g., a continental cap balanced over the South Pole will have a center of gravity at the South Pole, whereas the average latitude weighted by area will give a lower latitude value). Pangea formed at ~320 Ma, it had begun to break-up before the Paleozoic had ended (e.g., opening of the Neotethys Ocean, Fig. 11a) but most of Pangea was united until the Central Atlantic Ocean started to open between North America ("Laurussia") and Africa–South America

("Gondwana") at ~195 Ma and shortly after the emplacement of the CAMP (201 Ma). Note that the latitudinal component of the continental center of mass drifted slowly northwards with approximately the same velocity from 320 to 195 Ma, and thus unaffected by the formation of Pangea (see text). **(b)** Average absolute continental paleolatitude weighted by area (i.e. North and South values collapsed together). **(c)** Percent of the total continental area that lies in the tropics (between 23.5° N and S) as a function of time. **(d)** Average absolute evaporite latitudes (i.e. North and South values collapsed together). The mean evaporite latitude for the past 50 Myrs is 33 ± 11° (standard deviation; 25 Myr bin averages) but in deeper time mean latitudes are considerably lower. All calculations based on a paleomagnetic reference frame (Torsvik *et al.* 2014; Torsvik & Cocks 2017).
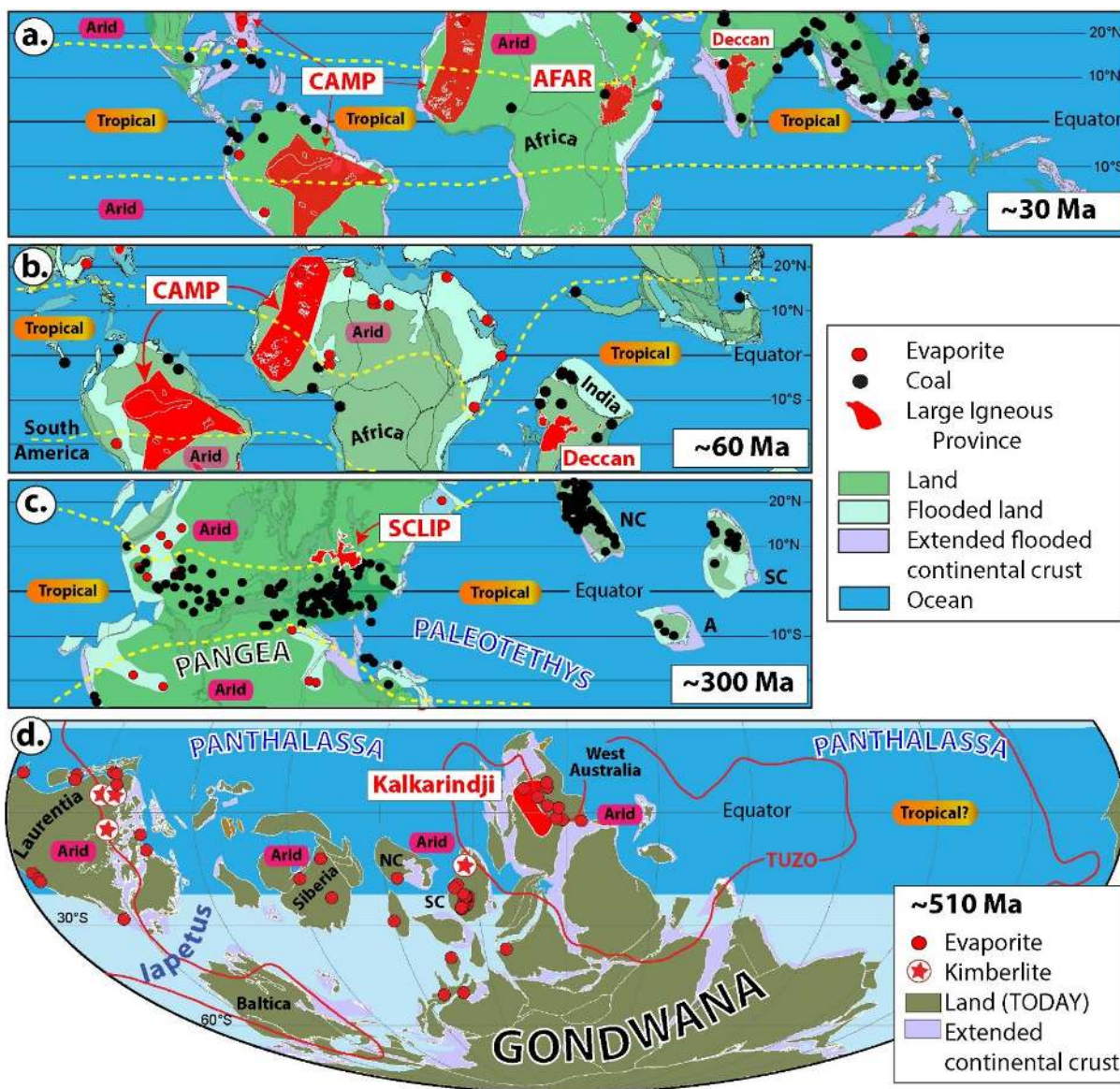
Figure 10 Reconstructed tropical belts at (**a**) 30 Ma, **(b)** 60 Ma and (**c**) 300 Ma along with occurrences of evaporite and coal, tentative outlines (yellow lines) of tropical climate (Torsvik & Cocks 2017; Boucot *et al.* 2013) and the outlines of the Central Atlantic Magmatic Province (CAMP), Deccan Traps, Afar (panels **a,b**) and the Skagerrak Centred LIP (SCLIP, panel **c**). We also indicate the areas of flooded land. (**d**) Earth geography in the Cambrian (~510 Ma) with restored occurrences of evaporites (Torsvik & Cocks 2017) and the outline of the Kalkarindji LIP. All reconstructions in a paleomagnetic frame and in panel **d** we also show the PGZs which have been counter-rotated (-49° around 0°N and 11°E; Torsvik *et al.* 2014) to account for estimated true polar wander at this time. A, Annamia (Indo-China); NC, North China; SC, South China.
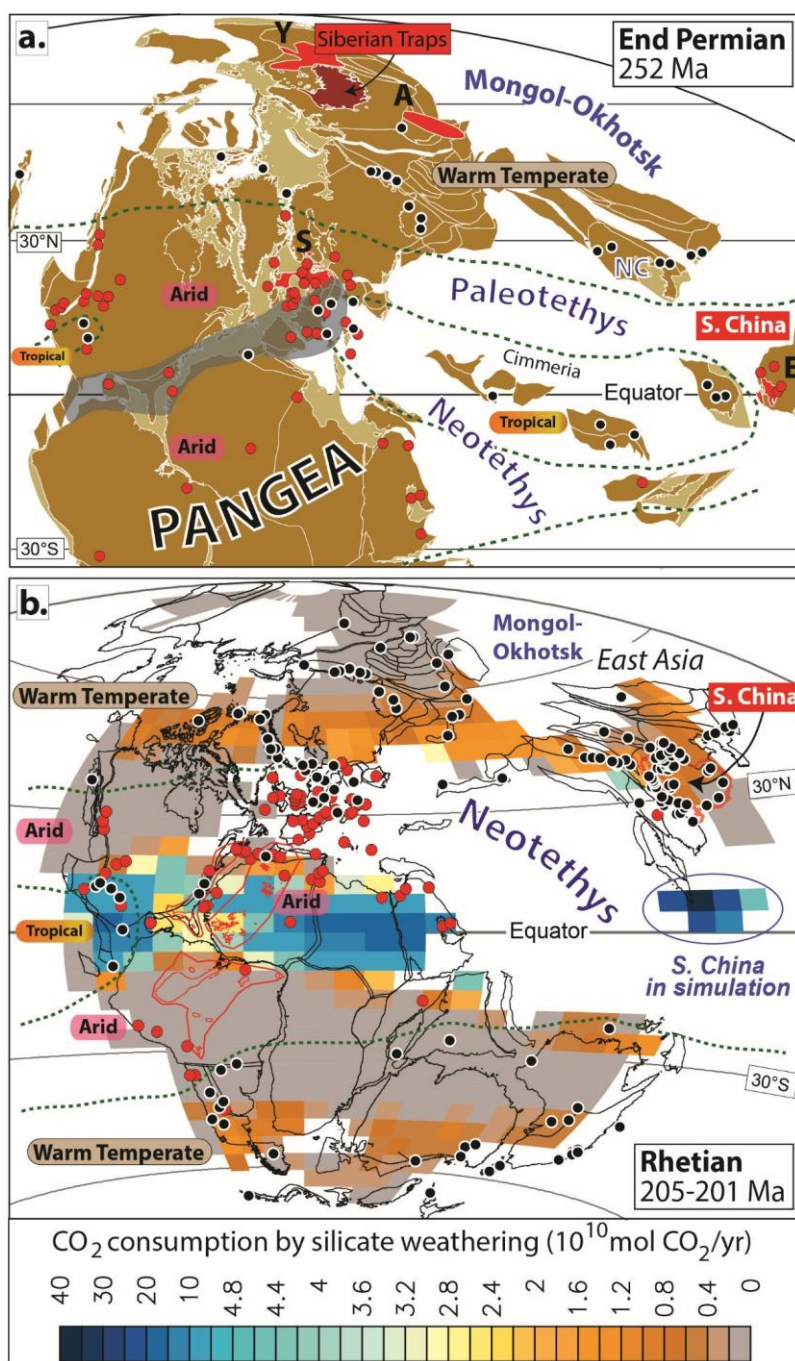
Figure 11 (**a**) End-Permian paleomagnetic reconstruction (252 Ma) and occurrences of evaporite (red shaded circles) and coal (black/white shaded circles), tentative climate-zone boundaries (green stippled lines) and outline of the areas affected by the Variscan and Alleghanian orogenies (dark shading) during Pangea formation. We also show the extent of the Siberian Traps (linked to mass extinction #3) but also the location of the Altay-Sayan (A), Emeishan (E); Skagerrak Centred LIP (S) and the Yakutsk (Y, linked to mass extinction #2) LIPs at this time. NC, North China. (**b**) Rhetian paleomagnetic reconstruction (205-201 Ma) with occurrences of evaporite (red shaded circles) and coal (black/white shaded circles), and tentative outlines of climate gradients. We also show the possible original extent of the Central Atlantic Magmatic Province (linked to mass extinction #4) at around 201 Ma (red lines). The estimated plume centre is near the southern tip of Florida. The reconstruction is compared with a Rhetian GEOCLIM simulation (Goddéris *et al.* 2014) with estimated CO_2 consumption from silicate weathering. The continental distribution (defined by the coloured and grey regions of continental *weatherability*) broadly matches our reconstruction (black lines). CO_2 consumption in the tropical parts of central Pangea is typically calculated to 10-20 x 10^{10} mol CO_2/yr whilst the warm temperate belts range between 1.4-1.8 x 10^{10} mol CO_2/yr. South China in the simulation is located near the Equator in the Neotethys – with CO_2 consumption estimates peaking at 40 x 10^{10} mol CO_2/yr.
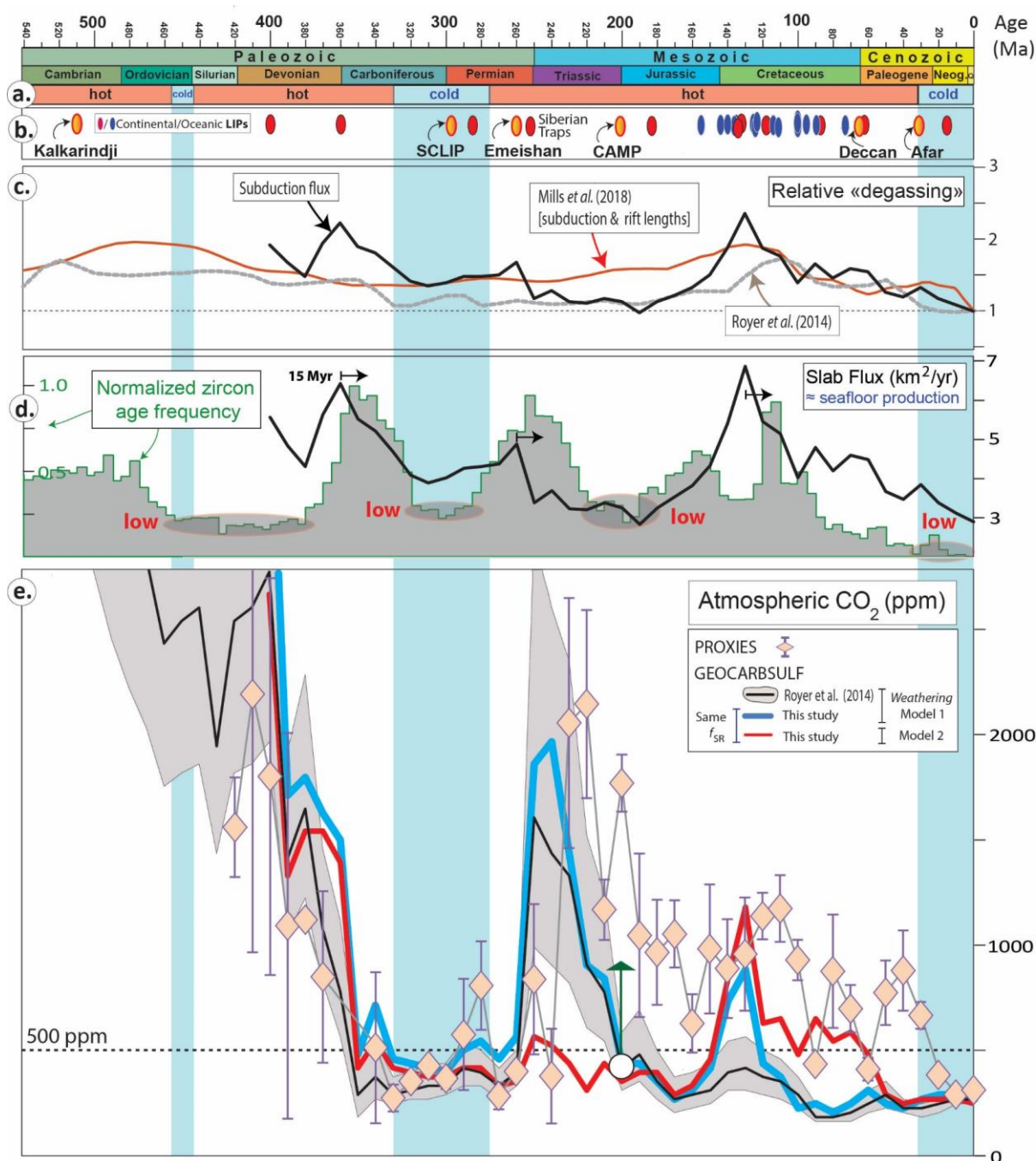
Figure 12 (a) Phanerozoic timescale with greenhouse (hot) *versus* icehouse (cold) conditions. **(b)** LIPs where Kalkarindji, Skagerrak Centred LIP (SCLIP), Emeishan (E), Central Atlantic Magmatic Province (CAMP), Deccan and Afar LIPs were emplaced at low latitudes (ST, Siberian Traps). Also indicated are the two kimberlite frequency peaks between 110-120 and 80-90 Ma (see Fig. 3f). **(c)** Relative CO_2 degassing (red curve, Mills *et al.* 2018) based on a combination of subduction [from seismic tomography for the past 200 Myrs (van der Meer *et al.* 2014) and a plate model before that time (Mills *et al.* 2017)] and continental rift lengths (Brune *et al.* 2017). Mills *et al.* (2018) assumed 37% (63%) of tectonic CO_2 contribution from continental rifts (ridges and arcs) and assumed constant rift input before 200 Ma. We also show relative degassing based on the global subduction flux (black curve) back to 400 Ma based on full-plate models (see Table 3 for details), and the standard GEOCARBSULF curve (f_{SR}) back to 541 Ma (grey curve; Royer et al. 2014). **(d)** Age frequency of detrital zircons from arc environments (frequency lows indicated with red ellipses) and subduction flux (black line; Table 3). Globally, the main peaks in the detrital zircon frequency distribution are shifted by ~15 Myrs (Domeier *et al.* 2018), i.e. zircons trailing subduction. **(e)** Atmospheric CO_2 proxies (binned in 10 Myr intervals with 95% confidence standard errors when

N≥2) since the Early Devonian (based on data used in Foster *et al.* 2017). GEOCARBSULF modelling (Royer *et al.* 2014) shown with 95% confidence area (shaded in grey) using the standard relative degassing curve (panel **c**) or CO_2 modelling (since 400 Ma) based on use of the subduction flux as a proxy for plate tectonic degassing (f_{SR}). The latter has been calculated using two different silicate weathering feedback models, i.e. Royer *et al.* (2014; blue line) and Berner (2006; red line). Weathering-related inputs in Royer et al. (2014) is based on Goddéris *et al.* (2012, 2014) but in the global runoff/weathering model South China was *misplaced* near the equator at 200 Ma and accounting for about 17% of the global CO_2 consumption by silicate weathering (see text and Fig. 11b). If the large "cooling" contribution from South China is removed, then modelled CO_2 would increase by around 500 ppm and better match the CO_2 proxies (green arrow at 200 Ma).